

## RESEARCH ARTICLE

# Growth control by a moving morphogen gradient during *Drosophila* eye development

Ortrud Wartlick<sup>1,\*</sup>, Frank Jülicher<sup>2,\*</sup> and Marcos Gonzalez-Gaitan<sup>1,\*</sup>

## ABSTRACT

During morphogenesis, organs grow to stereotyped sizes, but growth control mechanisms are poorly understood. Here, we measured the signaling dynamics of the morphogen Dpp, one of several *Drosophila* factors controlling morphogenetic growth, in the developing eye. In this tissue, the Dpp expression domain advances from the posterior to the anterior tissue edge. In front of this moving morphogen source, signaling inputs including Dpp activate the target gene *hairy* in a gradient that scales with tissue size. Proliferation, in turn, occurs in a mitotic wave in front of the source, whereas behind it, cells arrest and differentiate. We found that cells divide when their signaling levels have increased by around 60%. This simple mechanism quantitatively explains the proliferation and differentiation waves in wild type and mutants. Furthermore, this mechanism may be a common feature of different growth factors, because a Dpp-independent growth input also follows this growth rule.

**KEY WORDS:** Eye, Development, *Drosophila*, Morphogen, Growth, Models, Biophysics

## INTRODUCTION

For many years, *Drosophila* imaginal discs have been a model system of choice to study genetic mechanisms of patterning and growth control (Affolter and Basler, 2007). A key advance in this work was the identification of morphogen gradients, which coordinate growth and patterning. The morphogen Dpp, which forms graded concentration profiles in imaginal discs, is one of the major contributors to growth control in imaginal tissues. However, in the absence of Dpp input, there can still be growth, and target genes still show a graded distribution (Burke and Basler, 1996; Campbell and Tomlinson, 1999; Jazwinska et al., 1999; Wartlick et al., 2011b, 2012; Schwank et al., 2012). This indicates that Dpp contributes to a graded signal that controls growth, but it is not the only input. Because it is unclear what controls growth in the absence of Dpp, Dpp remains the best characterized growth signal (reviewed by Wartlick et al., 2011a). In this work, we therefore focus on Dpp. However, we also show that growth control mechanisms identified for Dpp may apply to other growth signals.

Based on quantitative measurements of Dpp gradient and growth dynamics of the wing disc, we previously proposed a temporal model

for morphogenetic growth control, in which cells divide whenever their morphogen levels have increased by about 50% since the beginning of the cell cycle (Wartlick et al., 2011b). Other models propose that growth is controlled by absolute morphogen levels, the slope of a signaling gradient, and/or inputs from tissue mechanics (Rogulja and Irvine, 2005; Shraiman, 2005; Aegerter-Wilmsen et al., 2007; Schwank et al., 2008; Hamaratoglu et al., 2009; Schwank and Basler, 2010). All these models, including the temporal model, have been proposed for the wing disc, and it is unknown if they could work in other developmental contexts. For example, the eye disc is strikingly different from the wing, yet Dpp also contributes to its growth (among other factors) (Burke and Basler, 1996; Penton et al., 1997; Horsfield et al., 1998; Baker, 2001; Firth et al., 2010).

The eye disc consists of a differentiating posterior and a proliferative anterior part, separated by the morphogenetic furrow, an epithelial constriction along the dorsoventral axis (Tomlinson, 1985; Baker, 2001). Cells in this furrow express Dpp, i.e. the furrow constitutes a Dpp source (Ma et al., 1993; Penton et al., 1997; Horsfield et al., 1998), and there is a Dpp signaling gradient along the anteroposterior axis (Firth et al., 2010). During development, the furrow sweeps across the tissue, from the posterior to the anterior end. Furrow movement is driven partly by Hedgehog (Hh) (Corrigall et al., 2007), which is secreted by posterior differentiating photoreceptor cells and also activates Dpp expression in the furrow (Heberlein et al., 1993, 1995; Ma et al., 1993; Strutt and Mlodzik, 1997; Dominguez, 1999; Greenwood and Struhl, 1999; Curtiss and Mlodzik, 2000). As posterior differentiation progresses, the resultant Hh gradient moves anteriorly, shifting the Dpp expression domain. Proliferation rates of anterior cells close to the furrow are high, but decrease with increasing distance. This proliferation pattern is called the first mitotic wave (Baker, 2001). Anterior cells entering the furrow transiently arrest in G1 (Wolff and Ready, 1991). As the furrow passes, some of these cells commit to one final, Dpp-independent round of cell division before differentiation, the posterior ‘second mitotic wave’ (Wolff and Ready, 1991; Brown et al., 1996; Dong et al., 1997; Baker, 2001; Firth and Baker, 2005; Yang and Baker, 2006).

This complex proliferation and differentiation pattern raises interesting questions about growth control. Indeed, Dpp is required for anterior proliferation, but also for G1 arrest in the furrow (Penton et al., 1997; Horsfield et al., 1998; Firth et al., 2010), implying two contradictory roles. It was suggested that anterior proliferation depends on absolute Dpp levels, and that G1 arrest is due to inhibition of proliferation above a Dpp threshold (Horsfield et al., 1998; Firth et al., 2010). However, this is inconsistent with some experimental findings (see below) and different from the role of Dpp in the wing disc.

Could the pattern of proliferation and arrest in the eye disc, which is so strikingly different from the wing with its static Dpp source and homogeneous proliferation, be explained by any of the growth models proposed for the wing? Interestingly, a moving morphogen

<sup>1</sup>Department of Biochemistry, Faculty of Sciences, University of Geneva, 30 Quai Ernest Ansermet, Geneva 1211, Switzerland. <sup>2</sup>Max Planck Institute for the Physics of Complex Systems, Nöthnitzer Strasse 38, 01187 Dresden, Germany.

\*Authors for correspondence (marcos.gonzalez@unige.ch, julicher@pks.mpg.de, o.wartlick@ucl.ac.uk)

This is an Open Access article distributed under the terms of the Creative Commons Attribution License (<http://creativecommons.org/licenses/by/3.0>), which permits unrestricted use, distribution and reproduction in any medium provided that the original work is properly attributed.

source should increase morphogen levels in front of it, while decreasing them in its wake, which *prima facie* could be consistent with anterior proliferation and posterior arrest and differentiation in the eye (Fig. 1A).

Here we quantified growth parameters and Dpp signaling gradients in the eye. First, we found that, as a consequence of furrow movement and tissue growth, the anterior tissue initially expands but later shrinks, as it is ‘consumed’ by the furrow. During tissue expansion, signaling gradients scale up to match tissue size, and, strikingly, tissue shrinkage is accompanied by scaling down of the gradient, challenging current models of gradient scaling (Ben-Zvi and Barkai, 2010; Ben-Zvi et al., 2011). Second, we developed a theory of growth control by temporal morphogen signaling (first proposed in the wing) for the strikingly different scenario in the eye, with a moving morphogen source. We show that the temporal model can explain the observed spatiotemporal patterns of wild-type eye growth in quantitative detail (Fig. 2). Third, using mutants affecting gradient shape, temporal gradient dynamics or the furrow velocity, we show that the temporal model quantitatively explains mutant-specific patterns of proliferation in all conditions (Figs 3 and 4). Finally, we found that this mechanism applies in the absence of Dpp input (Fig. 5), suggesting that temporal growth regulation may be a general mechanism.

## RESULTS

### Growth parameters and Dpp signaling dynamics

To understand eye growth and the relative contribution of Dpp-dependent and -independent growth control, we quantified growth and signaling dynamics during larval stages (supplementary material Table S1). From 40 h to 90 h after hatching, the linear dimensions of the eye disc increase fourfold, from 50 to 200  $\mu\text{m}$  in width ( $L_x$ ) and 100 to 400  $\mu\text{m}$  in height ( $L_y$ ) (Fig. 1). The total width  $L_x$  comprises the

widths of the posterior and anterior regions (Fig. 1C, right). The anterior width  $L_a$  initially increases, but eventually shrinks as the furrow incorporates anterior cells faster than they can proliferate (Fig. 1D). At the time of pupariation (about 96 h after hatching of the larva), furrow movement across the anterior is not yet completed, so some anterior tissue remains. From 60 h to the end of third instar, the posterior width  $L_p$  steadily increases by about  $v_s \approx 3 \mu\text{m}/\text{h}$  (Fig. 1D). This velocity  $v_s$  corresponds to the velocity of furrow progression, because the contribution of the posterior second mitotic wave to posterior width growth can be neglected (see the Materials and methods in the supplementary material). Finally, because anterior cell divisions are approximately isotropic with respect to the furrow boundary (Baena-López et al., 2005), the proliferation rate  $g$  is closely related to the growth rate in x-direction  $g_x$ :  $g = g_x(1 + \epsilon)$ , where the anisotropy,  $\epsilon = g_y/g_x$ , is approximately  $\epsilon \approx 1$  (Fig. 1E).

Tissue growth and source movement are accompanied by changes in signaling. To examine Dpp-dependent signaling as well as Dpp-independent signaling anterior to the furrow, we used two readouts: phosphorylated Mad (P-Mad), a Dpp signal transducer (Wiersdorff et al., 1996), and Hairy (Brown et al., 1991). Anterior Hairy expression is elevated by Dpp (Greenwood and Struhl, 1999), but Hairy also responds to other signals emanating from posterior cells, including Hh, Notch and other, unknown factors (Fu and Baker, 2003). Hairy thus serves as a general signaling readout anterior to the furrow. Because it is repressed in posterior cells, the Hairy signaling gradient also shifts with the furrow and indicates furrow position (Brown et al., 1991; Ma et al., 1993) (Fig. 1C, Fig. 2A). At the equator (a central, narrow region perpendicular to the furrow) and polar regions (the farthest edges of the eye disc parallel to the equator), P-Mad and Hairy profiles are often distorted (perhaps as a result of constriction, folding or boundary effects) (Fig. 1C), so we avoided these regions in the following analysis.

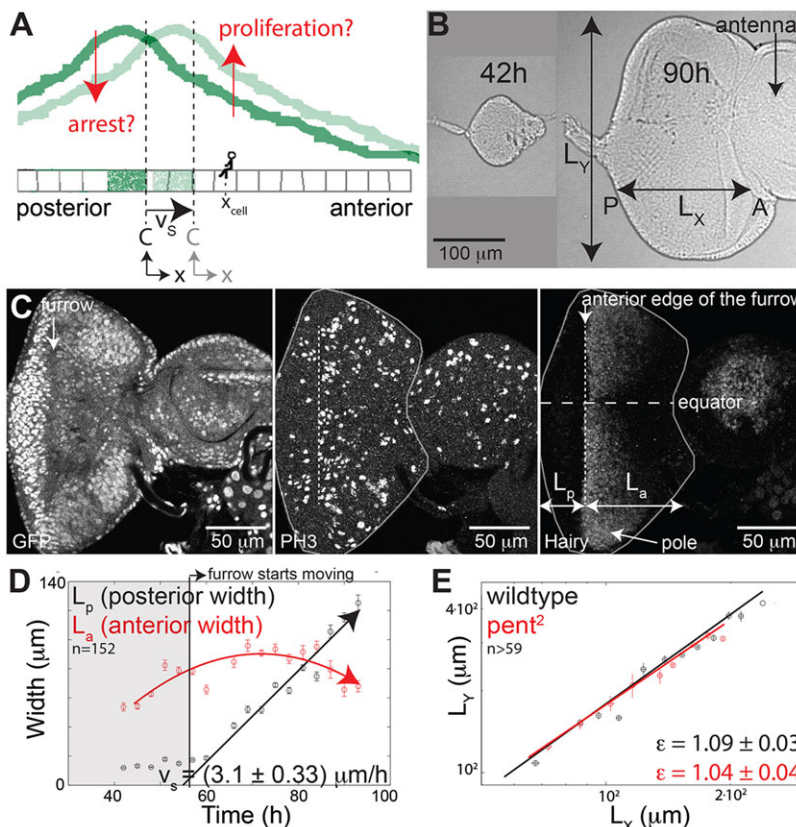


**Fig. 1. Growth dynamics in the eye imaginal disc.**

(A) Scheme of the eye disc along the anteroposterior axis, with idealised morphogen source (green expression domain) and gradient (green traces); due to movement of expression domain with velocity  $v_s$  towards the anterior, anterior cells experience increases in signaling levels over time, whereas posterior cells experience decreases in signaling levels. These changes in signaling could drive proliferation or arrest. Here and in the main text, the coordinate system moves together with the anterior source boundary (at  $x=0$ ); cells are positioned at a distance  $x_{cell}$  from this boundary and therefore move relative to the source. (B) Representative eye discs from 42 h and 90 h after hatching;  $L_x$  and  $L_y$  are the widths of the disc in x- and y-directions, respectively. (C) Wild-type eye imaginal disc with ubi-GFP, PH3 and Hairy stainings; Hairy marks the furrow boundary; anterior ( $L_a$ ) and posterior ( $L_p$ ) widths are indicated. Equatorial and polar regions were avoided for subsequent quantifications because their intensity profiles are distorted by constriction or folding. (D) Anterior (red) and posterior (black) width during development (arrows visualize trends); the furrow velocity ( $v_s$ ) can be extracted from a linear fit to the posterior width over time;  $n=152$ . E, anisotropy  $\epsilon$  is the ratio of growth rates in y- and x-directions.

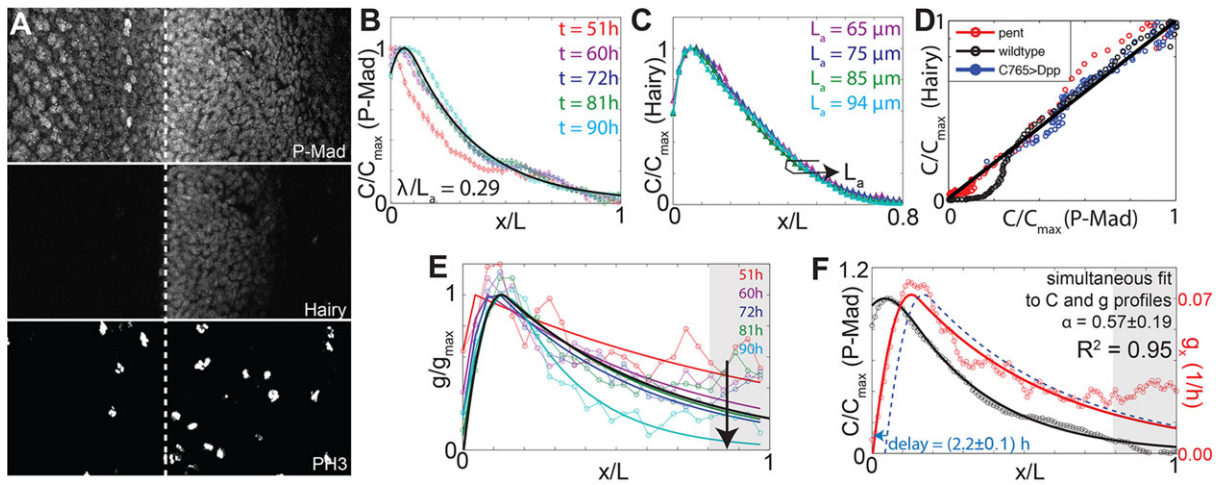


**Fig. 2. Signaling dynamics and growth.** (A–F) Wild type, from a dataset with  $n=152$ ; (A) Close-up of P-Mad, Hairy and PH3 stainings; dashed line: anterior edge of the furrow ( $x=0$ ); (B) Quantification of P-Mad profile shapes at different developmental times (in different colors); black line: fit to mean profile during time period for which the profiles scale (60–90 h for P-Mad); (C) Hairy profiles as in B, but binned by disc size ( $L_a$  bins chosen cover a time period from 51 to 90 h regardless of stage) to illustrate scaling: the profile shape is invariant. (D)  $C/C_{\max}$  of Hairy versus P-Mad, based on their spatial concentration profiles anterior to the peak in wild type, pent mutants and C765>Dpp discs; (E) As in B, for quantified PH3 profiles; black line: mean during 65–81 h, when the shape of the proliferation profile does not change very much. (F) Simultaneous fit to mean P-Mad (black) and proliferation profiles (red); blue: expected mitotic decision-making profile. After the decision to undergo mitosis is made (blue), a short time elapses (delay) before cells become PH3-positive (red); during this time interval cells move towards the posterior (from right to left); this explains the shift from blue to red profiles. The anteriormost 20% of the tissue were excluded from all fits (gray shaded areas). In this region,  $C(r)$  often has a steeper slope ( $\partial_x C$ ) than the fit function (black line), consistent with a higher level of proliferation (Eqn 6), so the model may explain the data in this region. However, there may also be distorting effects due to boundary conditions, folds, the influence of the antenna disc, or a failure to determine the anterior edge precisely (see also Fig. 1B).

We characterize anterior P-Mad and Hairy profiles by their amplitude  $C_{\max}$  and by a shape function  $f$  describing the position-dependence of the profiles anterior to the source:

$$C(x, t) = C_{\max}(t)f(x, t). \quad (1)$$

Here  $x$  is the distance to the anterior boundary of the moving source (Fig. 1A). Both P-Mad and Hairy are described by a function  $f$  that peaks ( $f=1$ ) close to the Dpp source, and decays with increasing distance. This decay is consistent with an exponential decay with a characteristic length  $\lambda_c$  (Fig. 2A–C; see Eqn 1 in the Materials and methods in the supplementary material).

### Upward and downward gradient scaling

Interestingly, when the experimental  $f_{P-Mad}$  and  $f_{Hairy}$  profiles are plotted as a function of relative position,  $r=x/L_a$ , they do not change during most of development. In particular, when gradient profiles from discs of similar anterior sizes are averaged and average profiles from differently sized discs are compared, it becomes apparent that  $f(x/L_a)$  does not depend explicitly on time, but rather on tissue size [ $f(x, t) \approx f(x/L_a(t))$ ] (Fig. 2B,C). In other words, signaling profiles scale with anterior tissue size: they expand and shrink (upward and downward scaling) proportional to changes of  $L_a$  during development, so that their relative shape is size- and time-independent. In addition, for both P-Mad and Hairy, the amplitude  $C_{\max}$  increases and decreases slightly with increasing and decreasing anterior tissue size,  $L_a$  (supplementary material Fig. S1B). These data are noisy, and changes in  $C_{\max}$  are most apparent when data are averaged according to anterior width (supplementary material Fig. S1C), indicating that changes in  $C_{\max}$  may reflect changes of the anterior width as a consequence of scaling and source movement. These findings are similar to the situation in the wing, where Dpp concentration and signaling gradients scale with increasing target tissue size (Lecuit and Cohen, 1998; Teleman and Cohen, 2000; Ben-Zvi et al., 2011;

Hamaratoglu et al., 2011; Wartlick et al., 2011a,b). However, the finding of downward scaling with a shrinking target challenges existing scaling models (see Discussion) (Ben-Zvi and Barkai, 2010; Ben-Zvi et al., 2011; Wartlick et al., 2011b).

To study how proliferation may correlate with these signaling dynamics, we also measured the spatial proliferation profile from the mitotic index (or mitotic density) determined by PH3 staining, which labels mitotic cells (Figs 1C and 2A,E). Anterior proliferation is strongly position-dependent: there is a peak of proliferation in front of the furrow (the first mitotic wave). Anterior to this peak, the growth rate decays with a characteristic decay length,  $\lambda_g$ . Growth profiles at later times are steeper than earlier ones (Fig. 2E).

We then studied the relationship between the spatiotemporal patterns of Dpp signaling and proliferation in the anterior, proliferative region of the eye disc. In the wing, a temporal model could explain the relationship between signaling and proliferation in quantitative terms. To study whether this model could work in the eye, we extended it to address the eye-specific geometry. We first discuss this temporal model and then discuss whether other growth models, such as growth control by absolute signaling levels or spatial slopes, can work in the eye.

### Theory of temporal growth control by a moving signaling gradient

We recently proposed a ‘temporal growth model’, where the growth rate  $g$  is determined by relative temporal increases in morphogen signaling levels as  $g=(\ln 2/\alpha)\dot{C}_{\text{cell}}/C_{\text{cell}}$ . Here  $\alpha$  describes the percentage by which signaling increases during one cell cycle. In the wing disc, the value of  $\alpha$  for a Dpp signaling output was estimated to be around 50% ( $\alpha=0.5$ ) (Wartlick et al., 2011b). The morphogen signaling level for a cell at position  $x_{\text{cell}}$  is defined as  $C_{\text{cell}}(t)=C(x_{\text{cell}}(t), t)$ , and  $\dot{C}_{\text{cell}}/C_{\text{cell}}$  is the rate of change in cellular morphogen signaling levels,  $\dot{C}_{\text{cell}}$ , relative to current levels  $C_{\text{cell}}$  (the dot in  $\dot{C}_{\text{cell}}$  denotes the time derivative). Taking a possible growth anisotropy  $\varepsilon$  into account (see



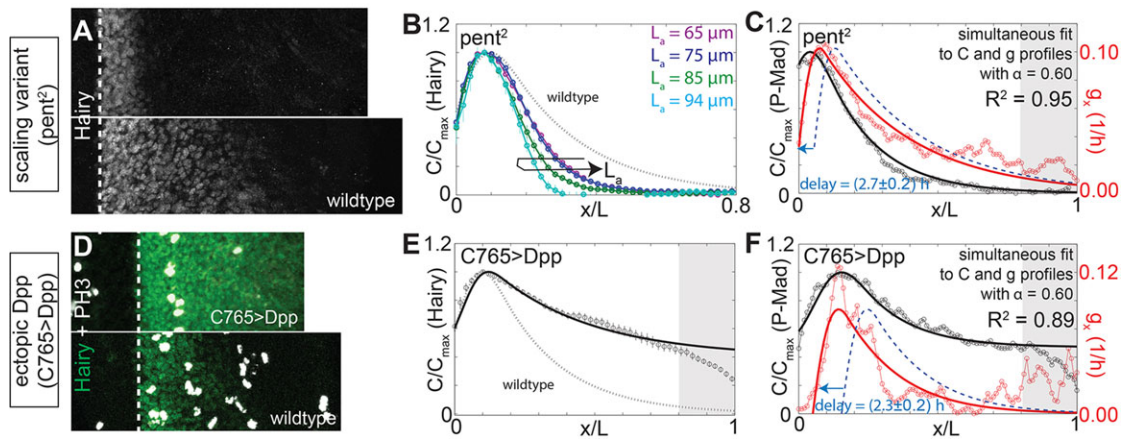


**Fig. 3. Mutants affecting gradient shape.** (A–C) *pent2* mutants, from a dataset with  $n=124$ ; (A,B) Hairy staining (A) and quantification (B; as in Fig. 2C); (C) as in Fig. 2F, with  $\alpha$  set to 0.60; D–F, C765>Dpp condition,  $n=20$ ; (D) Hairy (green) and PH3 (white) stainings; (E) Hairy quantification, (F) as in C. As in Fig. 2, the anteriormost 20% of the tissue were excluded from all fits (gray shaded areas) (see legend for Fig. 2).

above), the linear growth rate  $g_x$  is given by:

$$g_x = \gamma \frac{\dot{C}_{cell}}{C_{cell}} \quad \text{with} \quad \gamma = \frac{\ln 2}{\alpha(1 + \varepsilon)}. \quad (2)$$

Using Eqn 1, relative temporal changes in cellular morphogen signaling levels ( $\dot{C}_{cell}/C_{cell}$ ) are given by:

$$\frac{\dot{C}_{cell}}{C_{cell}} = \frac{\dot{C}_{max}}{C_{max}} + \left( v_{cell} - x_{cell} \frac{\dot{L}_a}{L_a} \right) \frac{\partial_x C}{C} \Big|_{x=x_{cell}}, \quad (3)$$

for a cell at distance  $x_{cell}$  from the anterior boundary of the source, moving relative to this boundary with velocity  $v_{cell} = \dot{x}_{cell}$  (Fig. 1A). In the eye,  $v_{cell}$  and  $\partial_x C$  are negative for most cells.

Eqn 3 shows that three effects contribute to changes of cellular signaling levels: cells experience an increase in signaling levels if the gradient amplitude  $C_{max}$  increases. This effect is position-independent. In addition, anterior cells experience an increase in signaling levels if they drift towards the source, i.e. upwards the signaling profile of slope  $\partial_x C$  with velocity  $v_{cell}$ . Finally, because the gradient scales with  $L_a$ , cells experience an increase (or decrease) in concentration if there is an increase (or decrease) in  $L_a$ , reflecting the expansion (or shrinking) of the gradient profile across the cell at position  $x_{cell}$ .

Anterior cells drift towards the morphogen source with velocity  $-v_S$  because the source moves anteriorly with velocity  $v_S$  (Fig. 1A), but at the same time, proliferation of other cells closer to the source will push a cell away from the source with velocity  $v_g$ , resulting in an effective cell velocity  $v_{cell} = v_g - v_S$ , where:

$$v_g(x_{cell}) = \int_0^{x_{cell}} g_x(x, t) dx. \quad (4)$$

Eqn 4 depends on cell position, because cells positioned farther away from the source can be pushed away by more proliferating cells. When the cell velocity  $v_{cell}$  is negative, cells are effectively approaching the morphogen source (Fig. 1A).

Note that Eqns 3 and 4 apply to both wing and eye discs; however, in the wing disc the source is static, i.e.  $v_S=0$ . Therefore, in the wing,  $v_{cell} \approx x_{cell} g_x$ , and thus  $v_{cell} = x_{cell} (\dot{L}_a/L_a)$ . As a consequence, the second term in Eqn 3 vanishes, implying

position-independent  $\dot{C}_{cell}/C_{cell}$  and homogeneous growth (Wartlick et al., 2011b). In the eye disc, the temporal model predicts that the second term of Eqn 3 generates strongly position-dependent growth, whereas the position-independent first term may initially increase, but later decrease proliferation rates overall, depending on changes in  $C_{max}$ .

We first consider the simple case in which we can neglect changes in  $L_a$  (i.e.  $\dot{L}_a=0$ ). If tissue size does not change,  $C_{max}$  does not change due to gradient scaling (i.e.  $\dot{C}_{max}=0$ ). Using Eqns 2 and 3 together with  $g_x = \partial_x v_g$  (from Eqn 4), we obtain a differential equation for the velocity profile due to growth:

$$\partial_x v_g = \gamma (v_g - v_S) \frac{\partial_x C}{C}. \quad (5)$$

Integration of Eqn 5 (see the Materials and methods in the supplementary material), leads to the proliferation profile:

$$g_x(x) = -v_S \partial_x \left( \frac{C(x)}{C_{max}} \right)^\gamma. \quad (6)$$

Eqn 6 shows that, in the temporal model, the spatial profile of proliferation depends on the source velocity and the spatial derivative of the normalized concentration profile: absolute signaling levels are not important. Eqn 6 predicts that, if the concentration profile is flat (the spatial derivative  $\partial_x C=0$ ), or if the source velocity is zero, then there is no proliferation. However, if  $C_{max}$  also changes in time, as taken into account in Eqn 3, an additional position-independent proliferation can occur. Note that Eqns 5 and 6 do not hold in the wing disc, because there the tissue steadily increases in size, and therefore  $\dot{L}_a > 0$  and  $\dot{C}_{max} > 0$ .

Eqn 6 is a good approximation for signaling and growth during developmental times from about 65 h to 85 h, because during this time, furrow progression approximately compensates for the widening of the target tissue due to growth. Therefore, target tissue size remains constant and the shape of the gradient is not changed by scaling. This means that  $\dot{L}_a \approx 0$  (Fig. 1D) and  $\dot{C}_{max} \approx 0$  (supplementary material Fig. S1B), and during these times the shape of the proliferation profile does not change much either (Fig. 2E).

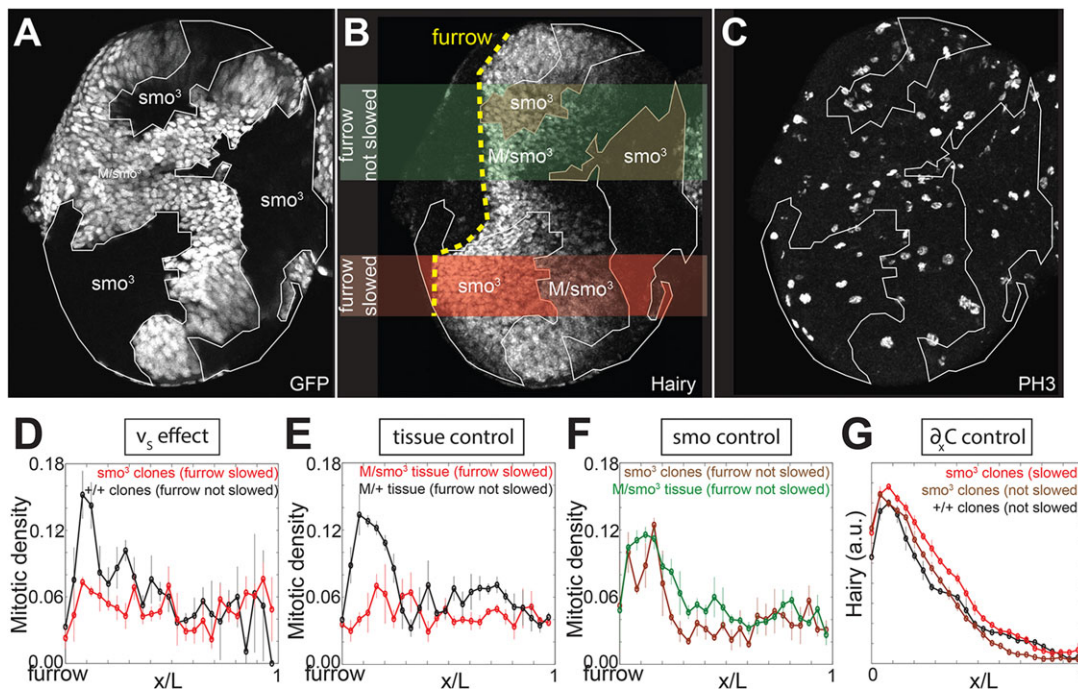


**Fig. 4. Mutants affecting the source velocity.** Sample sizes for clonal analyses are shown in supplementary material Fig. S1F. Note that, when the source velocity is small or zero, Eqn 6 does not apply, because  $L_a$  is no longer consumed by furrow movement, so simultaneous fits are not applicable. (A–C) Genotype: *yw hs-Flp; smo<sup>3</sup> FRT40A/M ubi-GFP FRT40A*; controls in f.g. *yw hs-Flp; FRT40A/M ubi-GFP FRT40A* (not shown in images); (A) *M<sup>+</sup> smo<sup>3</sup>* clones in *M/smo<sup>3</sup>* background, labeled by lack of GFP, with Hairy (B) and PH3 (C); the different types of *M<sup>+</sup> smo<sup>3</sup>* clones and analysed tissues are illustrated in B; (D–F) Spatial proliferation profiles as measured by PH3 staining for *M<sup>+</sup> smo<sup>3</sup>* clones (D; red) and *M/+* *smo<sup>3</sup>* tissue (E; red) in front of a retarded furrow (red stripe in B) compared with control tissue (black); (F) *M<sup>+</sup> smo<sup>3</sup>* clones (brown) and *M/+* *smo<sup>3</sup>* tissue (green) in front of a nonretarded furrow (green stripe in B) compared to control tissue; (G) Average Hairy gradient profiles for some of the conditions analyzed in D–F; all look similar but only the three most important profiles are shown. M, Minute.

### The temporal model accounts for the observed proliferation rates

Eqn 6 implies that the shape of the anterior proliferation profile depends on the shape of the signaling profile. We tested this by simultaneously fitting signaling and proliferation profiles, using Eqn 6 to constrain the fit functions (see the Materials and methods in the supplementary material). This simultaneous fit performs very well, for both P-Mad and Hairy signaling profiles ( $R^2=0.96$ ; supplementary material Fig. S1A), but slightly overestimates the distance between the peaks of P-Mad or Hairy profiles and the peak of the PH3 profile. This finding may indicate the existence of a delay between the commitment to undergo mitosis and the onset of PH3 expression, i.e. the onset of PH3 expression happens later and is therefore shifted posteriorly compared with the mitotic-decision-making event. We estimate this time delay to be about 2 h ( $R^2=0.97$ ; Fig. 2F, supplementary material Table S2). Taking this into account, we find that  $\alpha$  is approximately equal to 60% (Fig. 2F, supplementary material Table S2). Strikingly, in wild-type eye discs, the relative levels of Hairy and P-Mad are proportional to a large extent (Fig. 2D), i.e. although their amplitudes are different (supplementary material Fig. S1C), the shape of the relative signaling profiles is very similar (Fig. 2B–C), and as a consequence, the value of  $\alpha$  is similar for both ( $\alpha_{PMad}=0.57\pm0.19$ ,  $\alpha_{Hairy}=0.71\pm0.25$ ; supplementary material Table S2).

Remarkably, Eqn 6 not only accounts for the position of the mitotic peak (at the inflection point of the signaling profile), but also accurately predicts a region of growth arrest posterior to the signaling peak (Fig. 2F), where  $-\partial_x C$  becomes negative, resulting in negative  $\dot{C}_{cell}/C_{cell}$  and no proliferation. Furthermore, because the proliferation amplitude  $g_{max}$  and the source velocity are related (Eqn 6), we can obtain a value for the source velocity from the

simultaneous fit of signaling and growth profiles ( $v_S=2.9\text{ }\mu\text{m/h}$ ). This value is strikingly similar to the experimentally measured value ( $v_S=(3.1\pm0.3)\text{ }\mu\text{m/h}$ ; Fig. 1D). In other words, our theory predicts not only the spatial pattern of proliferation, but also the actual values of proliferation, consistent with the actual value of the source velocity. Eqn 6 was derived for the simple case in which  $\dot{L}_a\approx0$ , corresponding to the time period from 65 h to 85 h. However, the temporal model also accounts for proliferation rates when  $\dot{L}_a\neq0$  and  $\dot{C}_{max}\neq0$  (supplementary material Fig. S1D). A detailed analysis that takes data from times when  $\dot{L}_a\neq0$  and  $\dot{C}_{max}\neq0$  into account yields  $\alpha=0.59$  (supplementary material Fig. S1L–P and Movie 1).

### Testing the temporal model: I. mutants affecting gradient shape

To test Eqn 6, and the role of Dpp in growth control, we reduced the spatial range of the Dpp signaling gradient using the *pentagon* mutant (*pent<sup>2</sup>*). Pent (Magu – FlyBase) is a secreted Dpp-feedback regulator that influences gradient scaling in the wing, probably by decreasing Dpp degradation as a function of tissue size (Vuilleumier et al., 2010, 2011; Ben-Zvi et al., 2011; Hamaratoglu et al., 2011; Wartlick et al., 2011b). We found that, in the eye disc, scaling also depends on Pent: in *pent* mutants, both P-Mad and Hairy profiles are steeper than in wild type (Fig. 3A–C) and neither scale with  $L_a$  (cf. Figs 2C and 3B). Strikingly, relative levels of Hairy and P-Mad are still largely proportional (Fig. 2D). This indicates that, even though there are other inputs into the Hairy signaling gradient (Fu and Baker, 2003), when present, Dpp dominates the scaling, and thus the shape of the Hairy signaling profile. In the temporal model described by Eqn 6, growth is independent of absolute signaling



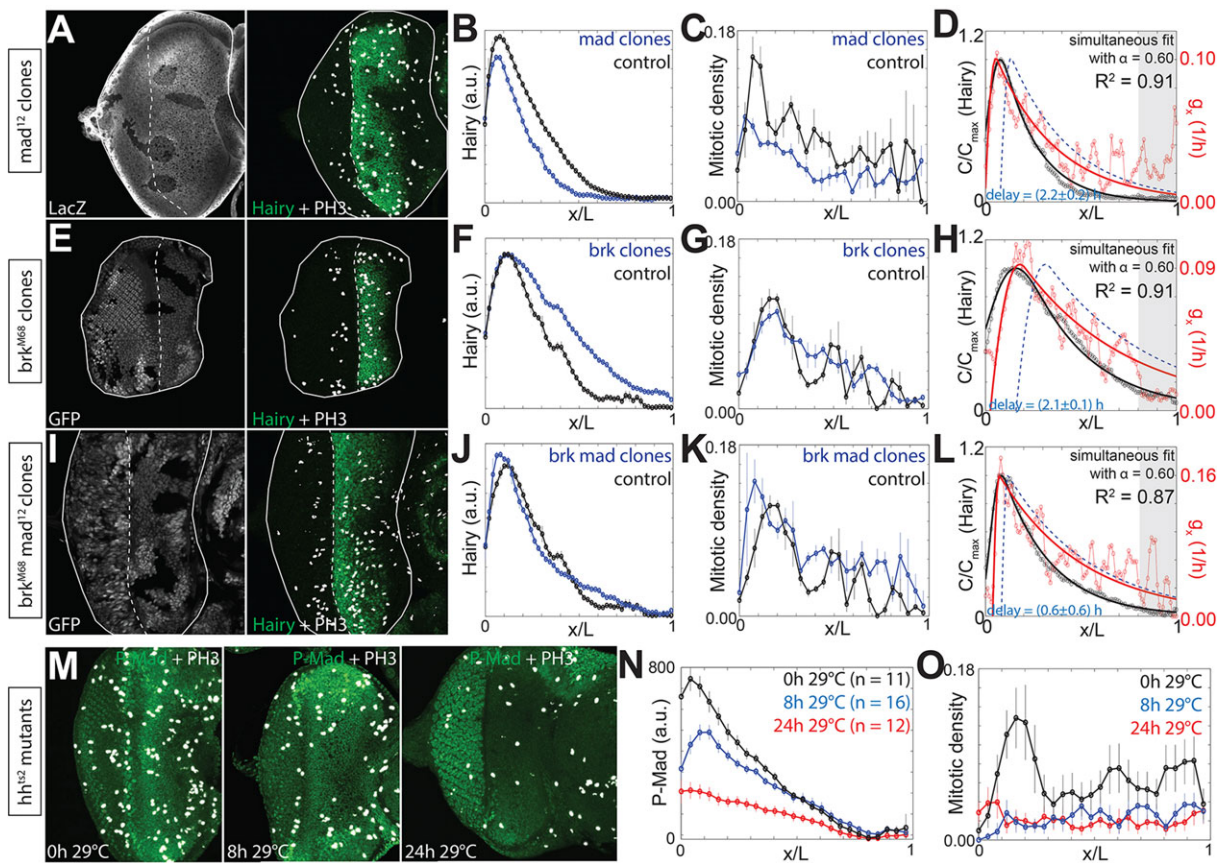


**Fig. 5. Dpp-independent proliferation, and growth arrest.** Sample sizes for clonal analyses are shown in supplementary material Fig. S1F. (A–D) *mad*<sup>12</sup> mutant clones; genotype: *yw hs-Flp*; *mad*<sup>12</sup> *FRT40A*/M *armZ* *FRT40A*; controls: wild-type clones from *yw hs-Flp*; *FRT40A*/M *ubi-GFP* *FRT40A*; (A) *mad*<sup>12</sup> clones marked by absence of *lacZ* (left) with Hairy and PH3 staining (right); (B,C) Hairy and growth quantification (note that the proliferation rate of *mad*<sup>12</sup> clones may be artificially high because they are grown in a Minute environment); (D) Simultaneous fit as in Fig. 2F, only with Hairy instead of P-Mad. (E–H) *brk*<sup>M68</sup> mutant clones; genotype: *brk*<sup>M68</sup> *yw hs-Flp*/Y; *FRT40A*/M *brk-rescue*<sup>BAC</sup> *ubi-GFP* *FRT40A*; controls: clones from *brk*<sup>M68</sup> *yw hs-Flp*/Y; *FRT40A*/M *brk-rescue*<sup>BAC</sup> *ubi-GFP* *FRT40A*; (E) *brk*<sup>M68</sup> clones marked by absence of GFP (left) with Hairy and PH3 staining (right); (F–H) as in B–D. I–L, *brk*<sup>M68</sup> *mad*<sup>12</sup> mutant clones; genotype: *brk*<sup>M68</sup> *yw hs-Flp*/Y; *mad*<sup>12</sup> *FRT40A*/M *brk-rescue*<sup>BAC</sup> *ubi-GFP* *FRT40A*; controls: as in E–H; (I) *brk*<sup>M68</sup> *mad*<sup>12</sup> clones marked by absence of GFP (left) with Hairy and PH3 staining (right); (J–L) as in B–D. In C, G and K, proliferation profiles are binned over position to visualize trends, whereas in D, H and L, the raw data are used for the fit. (M–O) *hh*<sup>ts2</sup> experiment; genotype: *hh*<sup>ts2</sup>, *e/UAS-HhCD2*, *hh*<sup>ts2</sup>, *e*; (the UAS-Hh-CD2 serves no purpose; the chromosome was used to avoid linked mutations); (M) sample images of *hh*<sup>ts2</sup> mutant discs after a shift to restrictive temperature; note that Dpp-independent P-Mad staining in differentiating posterior cells has been reported previously (Firth et al., 2010); images of controls are shown in supplementary material Fig. S1G; (N,O), P-Mad (N) and proliferation profiles (O) of *hh*<sup>ts2</sup> mutants at different times after the temperature shift (the quantification excluded the dorsal and ventral polar regions).

levels but rather depends on the *shape* of the signaling profile. Because of the linear relationship between Hairy and P-Mad, their profile shapes are equivalent and would therefore give rise to the same growth profile. Eqn 6 predicts that a steeper signaling profile should result in a steeper proliferation profile, if  $\alpha$  is unaffected. This is indeed experimentally observed: during a time period in which  $\dot{L}_a \approx 0$  (supplementary material Fig. S1E), in *pent* mutants, the shape of the proliferation profile is correctly predicted from both signaling profiles and consistent with a value of  $\alpha$  of 60% ( $R^2=0.97$  for both P-Mad and Hairy; Fig. 3C, supplementary material Table S2).

We next increased Dpp levels in all anterior cells by expressing Dpp ectopically using the C765-Gal4 driver. In the wing disc, expression of Dpp with C765-Gal4 led to *higher* proliferation rates laterally (far away from the source) (Schwank et al., 2008; Wartlick et al., 2011b). We showed that this effect can be quantitatively explained by a temporal model, because, in this condition, lateral cells experience higher relative increases in Dpp levels over time than medial cells, and therefore divide faster (Wartlick et al., 2011b). In eye discs, ectopic Dpp expression leads to *lower* lateral

proliferation rates than in wild type: the mitotic wave is sharper (Horsfield et al., 1998; Firth et al., 2010) (Fig. 3D–F). Yet this is also accurately predicted in quantitative terms by the temporal model: in C765>Dpp eye discs,  $-\partial_x(C(x))^\gamma$  far away from the source is smaller than in wild type because the signaling profile is flatter (for both P-Mad and Hairy signals, which are again proportional (Fig. 2D)). This substantially reduces proliferation there (Eqn 6). Again the shape and amplitude of the experimentally determined proliferation profile are consistent with  $\alpha=60\%$  ( $R^2=0.89$  for both P-Mad and Hairy; Fig. 3F, supplementary material Table S2).

Together, the *pent* and C765>Dpp experiments also show that absolute Dpp levels cannot control proliferation: in both cases, the proliferation profile is steeper than in wild type, although in one case there is ‘less’, and in the other, ‘more’ signaling (compare Figs 2F and 3C,F).

### Testing the temporal model: II. mutants affecting source movement

Another prediction of the temporal model is that position-dependent proliferation is a direct consequence of source movement (as

illustrated by Eqn 6). To test this, we generated large clones that encompass part of the furrow and are mutant for the Hh receptor Smoothed (Smo) (Fig. 4A–C). Furrow progression is severely retarded in these clones (Strutt and Mlodzik, 1997) (Fig. 4B). As predicted by a temporal model, proliferation in these clones is smaller and more homogeneous than in wild type (i.e. the mitotic wave disappears) (Fig. 4D). This result indicates that furrow movement causes the appearance of the mitotic wave.

Importantly, this effect is non-cell-autonomous: as predicted, nonmutant tissue in front of the retarded furrow also proliferates more homogeneously (Fig. 4E). Conversely, *smo*<sup>3</sup> clones that do not encompass the furrow and therefore do not slow it down retain the mitotic wave (Fig. 4F). Therefore, the lack of a mitotic peak in front of a retarded furrow cannot be explained by lack of Hh signaling. This is consistent with previous reports in which *smo*<sup>3</sup> clones were found to show a wild-type-like proliferation pattern, but their location was not taken into consideration (Escudero and Freeman, 2007). Finally, even when the furrow is retarded, causing suppression of the mitotic wave, the shape and amplitude of the Hairy signaling profile are comparable to controls (Fig. 4G): if the source does not move, a graded signaling profile cannot by itself cause position-dependent growth. These data are therefore inconsistent with two other morphogenetic growth models: control by absolute signaling levels or by the spatial slope alone.

### Dpp-independent proliferation also follows the temporal model

To test if the Dpp-independent contribution to growth is also velocity-dependent, i.e. if the growth response of cells to Dpp-independent growth signals still obeys a temporal rule, we generated *mad*<sup>12</sup>, *brk*<sup>M68</sup> and *brk*<sup>M68</sup> *mad*<sup>12</sup> mutant clones in the eye disc. Mad transduces Dpp input and Brk represses Dpp output (Affolter and Basler, 2007).

Mad mutant clones cannot normally be observed because they are outcompeted by surrounding cells. However, they do grow if generated in a Minute background, surrounded by slowly growing cells (Firth et al., 2010). In *mad*<sup>12</sup> mutant clones, the activation of *hairy* in the target tissue is reduced, but still graded (Fig. 5B), indicating that Dpp signaling contributes to hairy activation, but other inputs can generate a graded hairy profile. Although proliferation in *mad*<sup>12</sup> clones is reduced compared with controls, a mitotic wave is still observed (Fig. 5C). Interestingly, this proliferation profile is accurately predicted in quantitative terms by the Hairy profile according to Eqn 6 (Fig. 5D). This indicates that a Dpp-independent growth input into these cells is still present, and in the absence of Dpp, dominates the shape of the Hairy signaling profile and growth.

In *brk*<sup>M68</sup> clones, the proliferation profile is less steep, as predicted by their shallower Hairy profile (Fig. 5E–H), whereas *mad*<sup>12</sup> *brk*<sup>M68</sup> clones have a similar proliferation profile to controls, and strikingly, also have a wild-type-like Hairy profile (Fig. 5I–L). This suggests that the Brk mutation rescues growth in *mad*<sup>12</sup> clones by restoring the wild-type shape of the Hairy signaling profile in the absence of Dpp input. Interestingly, the delay between gradient readout and mitosis is much shorter in *mad*<sup>12</sup> *brk*<sup>M68</sup> clones. We do not know what molecular mechanism may drive this change.

Our results suggest that there is a spatially graded, Dpp-independent signal that also moves with the furrow (or is secreted from posterior cells) and drives growth via a temporal rule: as predicted by the temporal model, Dpp-independent proliferation is position-dependent for a moving source (in *mad*<sup>12</sup> clones), but position-independent for a non-moving source (in a *hh*<sup>ts</sup> experiment below). Furthermore, even in the absence of Dpp, the proliferation

profile can be predicted by the shape of the Hairy profile, and in all cases is consistent with  $\alpha=60\%$ . Thus the temporal model can offer an explanation both for Dpp-dependent and Dpp-independent growth in the eye disc.

### Growth arrest: negative values of $\dot{C}_{cell}/C_{cell}$ reduce proliferation

Our results so far show that the anterior proliferation profile in the eye can be explained by a temporal model. But what about growth arrest? In the temporal model, decreases in morphogen levels over time should stop cells from proliferating. This may happen naturally as anterior eye cells drift past the peak of signaling activity in front of the source (Figs 1A and 2F). Indeed, they also stop proliferating at least transiently, until Dpp-independent differentiation signals activate a program that includes a differentiative second wave of mitosis (Penton et al., 1997; Horsfield et al., 1998; Escudero and Freeman, 2007; Firth et al., 2010).

To test whether anterior cells in general respond to negative  $\dot{C}_{cell}/C_{cell}$  by arresting, we generated eye discs in which Dpp levels decrease everywhere, using Hh temperature-sensitive mutants (*hh*<sup>ts</sup>). When these mutants are shifted from the permissive (18°C) to the restrictive temperature (29°C), the furrow stops because no new Hh is produced, and the Dpp production rate decreases as the existing Hh gets degraded, resulting in decreased Dpp and Hairy expression (Ma et al., 1993). In this scenario, all cells are exposed to Dpp levels that decrease over time. We therefore quantified signaling and proliferation profiles in this condition to test whether negative  $\dot{C}_{cell}/C_{cell}$  causes growth arrest.

After 8 h at 29°C, P-Mad levels have decreased in the center, but not yet at the dorsal and ventral poles, where they do not decrease until 16 h and 24 h at 29°C (Fig. 5M,N). Consistent with a decrease in signaling levels over time, proliferation rates decrease dramatically, first in the center, and later in the whole tissue, although signaling levels are still high (Fig. 5M–O). This effect on proliferation is not observed in controls (supplementary material Fig. S1G). These results indicate that temporal decreases in signaling (negative  $\dot{C}_{cell}/C_{cell}$ ) correlate with a decrease in the proliferation rate. However, proliferation is not completely abolished – thus decreases in Dpp levels can contribute to growth arrest, but other factors must also contribute, consistent with previous reports (Horsfield et al., 1998).

### DISCUSSION

Our work provides a quantitative explanation of growth control by morphogen gradients. In summary, we make three fundamental observations: (1) eye growth is controlled by relative temporal changes in signaling levels, (2) Dpp-independent growth is also controlled by relative temporal changes in currently unidentified growth factor signals, and (3) gradient scaling is a universal feature of wing and eye discs. Notably, the growth rate expression derived for the temporal model in the eye disc (Eqn 6) does not only predict the overall shape of the spatial proliferation profile (a mitotic wave), but also the values of the observed proliferation rates.

### Growth is controlled by relative temporal changes in Dpp levels

What proliferation pattern results from temporal changes in signaling depends on the tissue configuration – a static source and scaling morphogen profile in the wing results in homogeneous proliferation (Wartlick et al., 2011b), whereas in the eye, a moving morphogen source generates a mitotic wave. In the wing, signaling increases over time because of gradient scaling (Wartlick et al., 2011b); in the eye, cells experience signaling increases because they

drift towards the morphogen source, up a graded concentration profile. Although the two tissues appear completely different at first glance, the growth of both can be accurately predicted by the same model.

Measurement of relative time derivatives ( $\dot{C}_{cell}/C_{cell}$ ) implies that adaptive responses are generated during the signaling event. An adaptive response allows cells to measure fold changes in a signal, because the signaling system adapts to ambient concentrations of the signal and increasing concentrations are necessary to elicit a response (reviewed by Alon, 2007). Adaptation operates during bacterial chemotaxis (Barkai and Leibler, 1997; Levchenko and Iglesias, 2002; Bargmann, 2006; Friedrich and Julicher, 2007), but adaptive responses were also observed in Wnt signaling in *Xenopus* (Goentoro and Kirschner, 2009) and have been proposed for a TGF $\beta$  signaling network (Vilar et al., 2006). How adaptive responses may be generated in the Dpp pathway remains unexplored. One speculation is that Dpp signaling could interact with another signaling system, such as the Hippo pathway, with which it could be wired in a network motif that can detect fold changes (Goentoro et al., 2009; Ma et al., 2009; Wartlick and González-Gaitán, 2011). However, more work will be necessary to dissect the molecular mechanism of temporal growth control.

### The temporal model holds beyond Dpp

Consistent with previous reports (Burke and Basler, 1996; Campbell and Tomlinson, 1999; Jazwinska et al., 1999; Schwank et al., 2012; Wartlick et al., 2012), we showed that there are Dpp-independent inputs into growth. These inputs are also graded in space and contribute to temporal changes in signaling that control growth. We can infer this because the Dpp-independent growth profile is still dependent on the source velocity (Fig. 5), which is predicted by the temporal model, but inconsistent with models that rely on absolute growth factor levels or spatial differences between cells. Interestingly, both Dpp-dependent and Dpp-independent growth profiles are accurately predicted by the Hairy profile. Notably, the absolute level of Hairy expression is not relevant; only its shape is important (Eqn 6). When present, Dpp dominates the Hairy profile shape: in wild type, by scaling it in a Pentagone-dependent manner, and in C765>Dpp by driving ectopic Hairy expression. Thus, in wild type, *pent* mutants and C765>Dpp discs, P-Mad and Hairy profile shapes are equivalent and predict the same proliferation pattern. By contrast, in *mad*<sup>12</sup> mutants, the Hairy profile shape is Dpp-independent, but strikingly still accurately predicts the Dpp-independent proliferation pattern. This suggests that, in the absence of Dpp, the Hairy profile shape reflects another growth signaling input. Indeed there are unknown, Dpp-independent inputs into Hairy expression (Fu and Baker, 2003).

### Gradient scaling

Scaling of the gradient is a universal feature of wing and eye discs, and Pentagone contributes to the scaling process, consistent with observations in the wing (Ben-Zvi et al., 2011; Hamaratoglu et al., 2011). Scaling is particularly intriguing in the eye disc, because the target tissue first grows and then shrinks, but the gradient stays proportional to tissue size. This upward and downward scaling challenges previously proposed scaling mechanisms (reviewed by Wartlick et al., 2011a). In a recently proposed scaling model based on an expansion/repression feedback (Ben-Zvi and Barkai, 2010; Ben-Zvi et al., 2011), scaling is controlled by the amount of a long-lived expander molecule, whose expression level is finely tuned: as the tissue size increases, the amount of expander steadily increases to expand the gradient. However, in the eye, when the target tissue

shrinks, the amount of expander would have to decrease quickly to shrink the gradient accordingly. This indicates that the expander cannot be long-lived (Ben-Zvi and Barkai, 2010; Ben-Zvi et al., 2011; Wartlick et al., 2011b). Thus current scaling models may have to be refined, for example, by additional feedbacks such as regulation of expander lifetime.

### Absolute morphogen levels or spatial differences in signaling between cells cannot explain proliferation patterns in the eye

We discussed the temporal growth model, in which cells divide in response to increases in morphogen signaling levels over time. However, our quantitative data also provide a test for other morphogenetic growth models. We have shown experimentally that a defining parameter of proliferation in the eye disc is the source velocity. In the temporal model, this parameter determines the emergence of a mitotic wave. By contrast, in models that rely on absolute morphogen levels or spatial differences in morphogen signaling between cells, the source velocity should have no effect. For example, if proliferation depended on absolute signaling levels, the proliferation profile should just mirror the signaling profile. This prediction is independent of the source velocity, and directly refuted by two of our experiments: (1) although signaling levels are high in C765>Dpp discs, proliferation is low and inhomogeneous, and its spatial pattern does not parallel the signaling profile (Fig. 3), and (2) when source movement is abolished, the mitotic wave disappears although signaling is still graded (Fig. 4). Therefore, proliferation cannot depend on absolute signaling levels or on an absolute signaling threshold.

What about spatial differences in signaling levels? A spatial growth model predicts that as long as there is a sufficiently steep signaling profile, there should be proliferation. Reducing the source velocity should have no impact, because the signaling profile is still graded. However, the proliferation profile is very strongly affected by reduction of the source velocity, even when the steepness of the signaling profile is close to the wild-type profile (Fig. 4). Therefore, global proliferation patterns in the eye disc cannot depend on spatial differences in signaling levels between cells alone. Spatial differences could, however, still play a role for proliferation in the context of wound healing or other scenarios (e.g. cell competition) where very sharp discontinuities in morphogen profiles are introduced.

### Mechanical stress could affect proliferation

Finally, proliferation could also depend on mechanical stress. Cells drifting towards the furrow do undergo shape changes (Corrigall et al., 2007). Reducing the furrow velocity could therefore have an effect on mechanical stress patterns in the tissue, which could directly affect proliferation or Dpp-independent growth signaling via mechanotransduction. However, inhomogeneous mechanical stress patterns related to source movement or inhomogeneous growth on their own cannot explain Dpp-dependent changes in proliferation, for example in *pent* mutants and in C765>Dpp discs (Fig. 3), where source movement is not significantly affected (supplementary material Table S2), although proliferation is dramatically affected but still inhomogeneous (Fig. 3). Indeed, it is not trivial to find a model that can explain the C765>Dpp data in the eye disc (lower proliferation far from the source), as well as the previously published data on C765>Dpp wing discs, in which opposite effects on proliferation were observed (higher proliferation far from the source). In our view, the effects on proliferation in both tissues together can only be explained by the temporal model.



## Conclusions

In summary, we propose a temporal growth model, in which cells divide in response to relative temporal increases in signaling inputs ( $\dot{C}_{cell}/C_{cell}$ ). In this way, proliferation rates can be precisely regulated (accelerated or decelerated) in time and space. We have shown that Dpp acts as one such growth regulator: in the wing disc, Dpp gradient scaling generates position-independent values of  $\dot{C}_{cell}/C_{cell}$  and homogeneous growth, whereas in the eye, source movement generates position-dependent patterns of  $\dot{C}_{cell}/C_{cell}$ , leading to position-dependent proliferation patterns. Furthermore, Dpp-independent growth signals also regulate growth according to a temporal growth rule. This could imply that temporal regulation is a common feature of growth regulatory signaling pathways. The observation that the value of the parameter  $\alpha$  in the case of the eye disc is similar for Dpp-dependent and Dpp-independent signals could indicate that different growth regulatory inputs may converge on a common biochemical network that translates  $\dot{C}_{cell}/C_{cell}$  into cell growth rates.

## MATERIALS AND METHODS

### Genetics

The following flies were used: Fig. 2, oregon[R]; Fig. 3A–C, pent[2]/CyO, act-GFP×pent[2]/CyO, act-GFP; Fig. 3D–F, C765-Gal4/TM3×UAS-GFP-Dpp/TM3; Fig. 4: yw hs-Flp; smo[3] FRT40A/CyO×M2(z) ubi-nGFP FRT40A/CyO, act-GFP (smo clones lack GFP); controls, yw hs-Flp; FRT40A/CyO×M2(z) ubi-GFP FRT40A/CyO, act-GFP; Fig. 5A–D: yw hs-Flp; mad[12] FRT40A/CyO act-GFP×w hs-Flp/Y; M arm[z] FRT40A/CyO act-GFP (mad clones lack *lacZ*); controls, yw hs-Flp; FRT40A/CyO×M2(z) ubi-GFP FRT40A/CyO, act-GFP; Fig. 5E–H, yw hs-Flp/Y; FRT40A/CyO×brk[M68] y w hs-Flp; brk[BAC rescue] ubi-GFP FRT40A/CyO (males have brk[M68] clones lacking GFP, females have ‘wild-type’ clones that are used as controls); Fig. 5I–L, yw hs-Flp/Y; mad[12] FRT40A/CyO×brk[M68], y w hs-Flp; brk[BAC rescue] ubi-GFP FRT40A/CyO (males have mad[12] brk[M68] clones lacking GFP; females have ‘wild-type’ clones that are used as controls); Fig. 5M–O: hh[ts2] e/TM6 ubiGFP×UAS-Hh-CD2 hh[ts2] e/TM6B (controls are siblings: hh[ts2] e/TM6B).

### Staging, fixation and antibody staining

Larvae were collected for 3 h per vial and were grown and dissected at specified times. Discs were fixed, stained and mounted as described previously (Entchev et al., 2000). Primary antibodies: rabbit anti Phospho-Smad3 (Epitomics 1880-1) – 1:100, mouse anti Hairy (Santa Cruz sc-53297) – 1:200, rat anti PH3 (Sigma H9908) – 1:5000, rabbit anti PH3 (Sigma H0412) – 1:5000.

### Image analysis, quantification procedures, fits and statistical analysis

Semi-automatic procedures for quantification and simultaneous fitting of gradient and mitotic density profiles in discs and clones were developed in MATLAB. These procedures are described in detail in the Materials and methods in the supplementary material.

Derivation of Eqns 3–6 and additional theoretical information is provided in the supplementary material.

### Acknowledgements

We thank N. Baker, M. Freeman, K. Basler, G. Pyrowolakis and S. Cohen for stocks and N. Baker for comments.

### Competing interests

The authors declare no competing financial interests.

### Author contributions

O.W., F.J. and M.G.-G. developed the project together.

### Funding

This work was supported by the Departement d'Instruction Publique of the Canton of Geneva, SNSF, the SystemsX epiPhysX grant, an ERC advanced

grant (Sara), the NCCR Frontiers in Genetics and Chemical Biology programs and the Polish-Swiss research program to M.G.-G. Deposited in PMC for immediate release.

### Supplementary material

Supplementary material available online at <http://dev.biologists.org/lookup/suppl/doi:10.1242/dev.105650/-/DC1>

### References

- Aegerter-Wilmsen, T., Aegerter, C. M., Hafen, E. and Basler, K. (2007). Model for the regulation of size in the wing imaginal disc of *Drosophila*. *Mech. Dev.* **124**, 318–326.
- Affolter, M. and Basler, K. (2007). The Decapentaplegic morphogen gradient: from pattern formation to growth regulation. *Nat. Rev. Genet.* **8**, 663–674.
- Alon, U. (2007). *An Introduction to Systems Biology: Design Principles of Biological Circuits*. London: Chapman & Hall/CRC Press, Taylor and Francis Group.
- Baena-López, L. A., Baonza, A. and García-Bellido, A. (2005). The orientation of cell divisions determines the shape of *Drosophila* organs. *Curr. Biol.* **15**, 1640–1644.
- Baker, N. E. (2001). Cell proliferation, survival, and death in the *Drosophila* eye. *Semin. Cell Dev. Biol.* **12**, 499–507.
- Bargmann, C. I. (2006). Chemosensation in *C. elegans* (October 25 2006), ed. The *C. elegans* Research Community, WormBook, doi:10.1895/wormbook.1.123.1, <http://www.wormbook.org>.
- Barkai, N. and Leibler, S. (1997). Robustness in simple biochemical networks. *Nature* **387**, 913–917.
- Ben-Zvi, D. and Barkai, N. (2010). Scaling of morphogen gradients by an expansion-repression integral feedback control. *Proc. Natl. Acad. Sci. U.S.A.* **107**, 6924–6929.
- Ben-Zvi, D., Pyrowolakis, G., Barkai, N. and Shilo, B. Z. (2011). Expansion-repression mechanism for scaling the Dpp activation gradient in *Drosophila* wing imaginal discs. *Curr. Biol.* **21**, 1391–1396.
- Brown, N. L., Sattler, C. A., Markey, D. R. and Carroll, S. B. (1991). hairy gene function in the *Drosophila* eye: normal expression is dispensable but ectopic expression alters cell fates. *Development* **113**, 1245–1256.
- Brown, N. L., Paddock, S. W., Sattler, C. A., Cronmiller, C., Thomas, B. J. and Carroll, S. B. (1996). daughterless is required for *Drosophila* photoreceptor cell determination, eye morphogenesis, and cell cycle progression. *Dev. Biol.* **179**, 65–78.
- Burke, R. and Basler, K. (1996). Hedgehog-dependent patterning in the *Drosophila* eye can occur in the absence of Dpp signaling. *Dev. Biol.* **179**, 360–368.
- Campbell, G. and Tomlinson, A. (1999). Transducing the Dpp morphogen gradient in the wing of *Drosophila*: regulation of Dpp targets by brinker. *Cell* **96**, 553–562.
- Corrigan, D., Walther, R. F., Rodriguez, L., Fichelson, P. and Pichaud, F. (2007). Hedgehog signaling is a principal inducer of Myosin-II-driven cell ingression in *Drosophila* epithelia. *Dev. Cell* **13**, 730–742.
- Curtiss, J. and Mlodzik, M. (2000). Morphogenetic furrow initiation and progression during eye development in *Drosophila*: the roles of decapentaplegic, hedgehog and eyes absent. *Development* **127**, 1325–1336.
- Dominguez, M. (1999). Dual role for Hedgehog in the regulation of the proneural gene atonal during ommatidia development. *Development* **126**, 2345–2353.
- Dong, X., Zavitz, K. H., Thomas, B. J., Lin, M., Campbell, S. and Zipursky, S. L. (1997). Control of G1 in the developing *Drosophila* eye: rca1 regulates Cyclin A. *Genes Dev.* **11**, 94–105.
- Entchev, E. V., Schwabedissen, A. and González-Gaitán, M. (2000). Gradient formation of the TGF-beta homolog Dpp. *Cell* **103**, 981–992.
- Escudero, L. M. and Freeman, M. (2007). Mechanism of G1 arrest in the *Drosophila* eye imaginal disc. *BMC Dev. Biol.* **7**, 13.
- Firth, L. C. and Baker, N. E. (2005). Extracellular signals responsible for spatially regulated proliferation in the differentiating *Drosophila* eye. *Dev. Cell* **8**, 541–551.
- Firth, L. C., Bhattacharya, A. and Baker, N. E. (2010). Cell cycle arrest by a gradient of Dpp signaling during *Drosophila* eye development. *BMC Dev. Biol.* **10**, 28.
- Friedrich, B. M. and Julicher, F. (2007). Chemotaxis of sperm cells. *Proc. Natl. Acad. Sci. U.S.A.* **104**, 13256–13261.
- Fu, W. and Baker, N. E. (2003). Deciphering synergistic and redundant roles of Hedgehog, Decapentaplegic and Delta that drive the wave of differentiation in *Drosophila* eye development. *Development* **130**, 5229–5239.
- Goentoro, L. and Kirschner, M. W. (2009). Evidence that fold-change, and not absolute level, of beta-catenin dictates Wnt signaling. *Mol. Cell* **36**, 872–884.
- Goentoro, L., Shoval, O., Kirschner, M. W. and Alon, U. (2009). The incoherent feedforward loop can provide fold-change detection in gene regulation. *Mol. Cell* **36**, 894–899.
- Greenwood, S. and Struhl, G. (1999). Progression of the morphogenetic furrow in the *Drosophila* eye: the roles of Hedgehog, Decapentaplegic and the Raf pathway. *Development* **126**, 5795–5808.
- Hamaratoglu, F., Basler, K. and Affolter, M. (2009). Confronting morphogen gradients: how important are they for growth? *Sci. Signal.* **2**, p e67.

- Hamaratoglu, F., de Lachapelle, A. M., Pyrowolakis, G., Bergmann, S. and Affolter, M.** (2011). Dpp signaling activity requires Pentagone to scale with tissue size in the growing *Drosophila* wing imaginal disc. *PLoS Biol.* **9**, e1001182.
- Heberlein, U., Wolff, T. and Rubin, G. M.** (1993). The TGF beta homolog dpp and the segment polarity gene hedgehog are required for propagation of a morphogenetic wave in the *Drosophila* retina. *Cell* **75**, 913-926.
- Heberlein, U., Singh, C. M., Luk, A. Y. and Donohoe, T. J.** (1995). Growth and differentiation in the *Drosophila* eye coordinated by hedgehog. *Nature* **373**, 709-711.
- Horsfield, J., Penton, A., Secombe, J., Hoffman, F. M. and Richardson, H.** (1998). decapentaplegic is required for arrest in G1 phase during *Drosophila* eye development. *Development* **125**, 5069-5078.
- Jazwinska, A., Rushlow, C. and Roth, S.** (1999). The role of brinker in mediating the graded response to Dpp in early *Drosophila* embryos. *Development* **126**, 3323-3334.
- Lecuit, T. and Cohen, S. M.** (1998). Dpp receptor levels contribute to shaping the Dpp morphogen gradient in the *Drosophila* wing imaginal disc. *Development* **125**, 4901-4907.
- Levchenko, A. and Iglesias, P. A.** (2002). Models of eukaryotic gradient sensing: application to chemotaxis of amoebae and neutrophils. *Biophys. J.* **82**, 50-63.
- Ma, C., Zhou, Y., Beachy, P. A. and Moses, K.** (1993). The segment polarity gene hedgehog is required for progression of the morphogenetic furrow in the developing *Drosophila* eye. *Cell* **75**, 927-938.
- Ma, W., Trusina, A., El-Samad, H., Lim, W. A. and Tang, C.** (2009). Defining network topologies that can achieve biochemical adaptation. *Cell* **138**, 760-773.
- Penton, A., Selleck, S. B. and Hoffmann, F. M.** (1997). Regulation of cell cycle synchronization by decapentaplegic during *Drosophila* eye development. *Science* **275**, 203-206.
- Rogulja, D. and Irvine, K. D.** (2005). Regulation of cell proliferation by a morphogen gradient. *Cell* **123**, 449-461.
- Schwank, G. and Basler, K.** (2010). Regulation of organ growth by morphogen gradients. *Cold Spring Harb. Perspect. Biol.* **2**, a001669.
- Schwank, G., Restrepo, S. and Basler, K.** (2008). Growth regulation by Dpp: an essential role for Brinker and a non-essential role for graded signaling levels. *Development* **135**, 4003-4013.
- Schwank, G., Yang, S.-F., Restrepo, S. and Basler, K.** (2012). Comment on "Dynamics of dpp signaling and proliferation control". *Science* **335**, 401.
- Shraiman, B. I.** (2005). Mechanical feedback as a possible regulator of tissue growth. *Proc. Natl. Acad. Sci. U.S.A.* **102**, 3318-3323.
- Strutt, D. I. and Mlodzik, M.** (1997). Hedgehog is an indirect regulator of morphogenetic furrow progression in the *Drosophila* eye disc. *Development* **124**, 3233-3240.
- Teleman, A. A. and Cohen, S. M.** (2000). Dpp gradient formation in the *Drosophila* wing imaginal disc. *Cell* **103**, 971-980.
- Tomlinson, A.** (1985). The cellular dynamics of pattern formation in the eye of *Drosophila*. *J. Embryol. Exp. Morphol.* **89**, 313-331.
- Vilar, J. M. G., Jansen, R. and Sander, C.** (2006). Signal processing in the TGF-beta superfamily ligand-receptor network. *PLoS Comput. Biol.* **2**, e3.
- Vuilleumier, R., Springhorn, A., Patterson, L., Koidl, S., Hammerschmidt, M., Affolter, M. and Pyrowolakis, G.** (2010). Control of Dpp morphogen signalling by a secreted feedback regulator. *Nat. Cell Biol.* **12**, 611-617.
- Vuilleumier, R., Affolter, M. and Pyrowolakis, G.** (2011). Pentagone: patrolling BMP morphogen signaling. *Fly (Austin)* **5**, 210-214.
- Wartlick, O. and González-Gaitán, M.** (2011). The missing link: implementation of morphogenetic growth control on the cellular and molecular level. *Curr. Opin. Genet. Dev.* **21**, 690-695.
- Wartlick, O., Mumcu, P., Jülicher, F. and Gonzalez-Gaitan, M.** (2011a). Understanding morphogenetic growth control – lessons from flies. *Nat. Rev. Mol. Cell Biol.* **12**, 594-604.
- Wartlick, O., Mumcu, P., Kicheva, A., Bittig, T., Seum, C., Jülicher, F. and Gonzalez-Gaitan, M.** (2011b). Dynamics of Dpp signaling and proliferation control. *Science* **331**, 1154-1159.
- Wartlick, O., Mumcu, P., Jülicher, F. and Gonzalez-Gaitan, M.** (2012). Response to Comment on "dynamics of Dpp signaling and proliferation control". *Science* **335**, 401.
- Wiersdorff, V., Lecuit, T., Cohen, S. M. and Mlodzik, M.** (1996). Mad acts downstream of Dpp receptors, revealing a differential requirement for dpp signaling in initiation and propagation of morphogenesis in the *Drosophila* eye. *Development* **122**, 2153-2162.
- Wolff, T. and Ready, D. F.** (1991). The beginning of pattern formation in the *Drosophila* compound eye: the morphogenetic furrow and the second mitotic wave. *Development* **113**, 841-850.
- Yang, L. and Baker, N. E.** (2006). Notch activity opposes Ras-induced differentiation during the Second Mitotic Wave of the developing *Drosophila* eye. *BMC Dev. Biol.* **6**, 8.

## Supplementary Material and Methods

### Quantification of disc parameters, intensity and mitotic density profiles in discs

Image stacks were projected using a maximum projection and despeckled in ImageJ. Occasionally, when a rat-anti-PH3 antibody had to be used in combination with m-anti-Hairy, there was some bleed-through of PH3 into Hairy. This bleed-through was removed using the outlier tool in ImageJ. Images were then loaded into **matlab** for further analysis.

The position of the furrow and a rectangular region of interest (ROI) were marked on the image by selecting two points on the posterior edge of the Hairy expression domain. The equatorial and polar regions were avoided, because the gradient is compressed or stretched in these regions (Firth et al. 2010) (Fig. 1C). The **furrow position** is the mean column value of positions of the two selected points. (A column on the image corresponds to a position along the anteroposterior axis.)

The values of pixels outside of the disc were set to NaN (not a number), so that they do not contribute to the following analysis.

The **posterior width** is approximately given by the mean number of non-NaN pixels per ROI row posterior to the furrow position times the image spacing ( $\mu\text{m}/\text{pixel}$  conversion factor). The **anterior width** is determined analogously using the non-NaN pixels located in anterior ROI rows. The **total width** is the sum of the two. The **intensity profiles** of P-Mad and Hairy are given by the mean intensity of the non-



NaN pixels per ROI column. Background was measured and subtracted from the resultant intensity profiles.

The P-Mad **background** was determined as the intensity level at the anterior edge of the disc. This seems to be accurate since in  $hh^{ts}$  mutants, after 24h at 29°C, there still is background staining at the edge, of the same intensity as in mutants after 0h at 29°C (not shown). Hairy background was determined in the posterior part of the disc, where Hairy is not expressed. Background was subtracted before fitting (see below).

The **mitotic density profile** was quantified analogously, except that the projected PH3 image was binarised before analysis, i.e. values of pixels outside the disc were set to NaN, values of PH3-positive pixels were set to 1, and all others were set to 0. To avoid discrepancies between different stainings or imagings, a general procedure was developed. This procedure adjusts the binarisation threshold in such a way that the binarisation always leads to similarly sized PH3-positive spots, regardless of the original image (Fig. S1H,I). The procedure is iterative: at each step, the mean area of PH3-positive spots in the image is determined. If it is bigger than a fixed optimal value, the binarisation threshold is increased, until the mean area of spots is close to the optimal value.

The mitotic density profile was then converted into a **growth rate profile**. To find the conversion factor, we made use of the fact that the measured mean tissue growth rate in x-direction,  $\bar{g}_x = \dot{L}_x / L_x$ , must be equal to the integral of the PH3 profile times a

conversion factor  $\kappa_x$ ,  $\kappa_x = \frac{\dot{L}_x / L_x}{\left( \int_0^{L_x} dx (PH3(x)) \right) / L_x}$ . Using this expression we find that the

value of  $\kappa_x$  is between  $0.75 \text{ h}^{-1}$  and  $1 \text{ h}^{-1}$  (Fig. S1J). Because the mitotic density is approximately equal to the duration of mitosis  $\theta_M$  divided by the cell doubling time  $\theta$ ,  $PH3 = \theta_M / \theta$ , and because the growth rate is inversely proportional to the cell doubling time:  $g = \ln 2 / \theta$ , the conversion factor  $\kappa_x$  is also given by  $\kappa_x = \ln 2 / (\theta_M (1 + \varepsilon))$ . For a value of  $\kappa_x$  between  $0.75 \text{ h}^{-1}$  and  $1 \text{ h}^{-1}$ , and a measured  $\varepsilon \approx 1$ , this yields a duration of mitosis  $\theta_M$  of between 21 and 28 minutes, which is in good agreement with experimental observations. For simplicity, from hereon we use  $\kappa_x \approx 1 \text{ h}^{-1}$  to convert PH3 profiles into  $g_x$  profiles.

Finally, all profiles were shifted by (imageSize – furrowPosition) so that all profiles aligned with respect to their furrow positions (at  $x = 0$ ). For the **mean profiles** shown, aligned profiles were normalised to their amplitude, and the mean profile shape with standard errors was determined for each time-point, for a group of time-points or for a group of discs as a function of relative position ( $r = x / L_a$ ).

### **Quantification of intensity and mitotic density profiles in clones**

For smo[3], mad[12], brk[M68] and mad[3] brk[M68] clones, larvae were heat-shocked at 60h after egg laying for 1 hour at  $37^\circ\text{C}$ . Larvae were dissected approximately three days later and fixed and stained as described above. Wherever possible, an internal control was chosen (e.g. measurements inside clones were compared to measurements outside clones but in the same discs) to minimize effects of stainings on the analysis.

Intensity and mitotic density profiles were quantified as described above, with the following difference. As above, the PH3 image was binarised, and the Hairy and PH3 values of pixels located outside the disc were set to NaN. In addition, a mask (a separate image) was created where values of pixels located inside clones were set to 1, and values of pixels outside clones were set to 0. There are therefore different pixel value combinations, notated as follows: NaN pixels are located outside of the disc, “(non – NaN, mask = 1)” pixels are located inside clones, and “(non – NaN, mask = 0)” pixels are located outside clones but inside the disc.

To analyse Hairy intensity and mitotic density **inside clones**, the intensity or mitotic density values were obtained as described above but using only the (non – NaN, mask = 1) pixels of each column of the chosen ROI. For those columns of the ROI for which there weren't any (non – NaN, mask = 1) pixels, for example if all the pixels of a column were located outside clones, the resultant values at that position were set to NaN. To analyse Hairy intensity and mitotic density **outside clones**, the same analysis was performed using the (non – NaN, mask = 0) pixels. Because clones never span a whole ROI, the sample size (number of clones contributing to the intensity or mitotic density values at a position) is different for each position (Fig. S1F).

### **Fitting of the theory to signaling intensity and mitotic density profiles**

The amplitude of signaling profiles was determined directly for each profile as the maximum obtained from a smoothing spline fit. To determine the shape of profiles, the normalized profiles,  $C(x)/C_{\max} = f_c(x)$ , were fit by a custom fit function. This fit function has to fulfill the following requirements: it has a maximum, an exponential



tail, and it has to scale with  $L_a$ , so that its shape is constant when plotted over relative position. We constructed a fit function of the form:  $C(x) = C_{\max} e^{-\int_0^x \lambda^{-1}(x) dx}$ . Here, the inverse of the decay length,  $\lambda^{-1}$ , is a function of  $x$ . It is chosen such that it is zero at the position of the signaling peak,  $x = x_c$ , accounting for the maximum, but constant for  $x > x_w$ , accounting for the exponential tail (Fig. S1K). These properties are obeyed by the following function  $f_c(x)$ :

$$f_c(x) = \begin{cases} e^{\frac{(x-x_c-x_w)^3}{3\lambda_c x_w^2} - \frac{(x-x_c-x_w)}{\lambda_c} - \frac{2x_w}{3\lambda_c}} & \text{for } 0 \leq x \leq x_c + x_w \\ e^{-\frac{(x-x_c-x_w)}{\lambda_c} - \frac{2x_w}{3\lambda_c}} & \text{for } x > x_c + x_w \end{cases} \quad (\text{supplementary equation 1}).$$

The function is piece-wise but continuous. At  $x = x_c$ ,  $f_c(x_c) = 1$  takes a maximal value so that  $C(x_c) = C_{\max}$ . Therefore,  $x_c$  is the position of the maximum of the concentration profile;  $x_w$  is the distance between this maximum and the start of the exponential tail of the profile;  $\lambda_c$  is the decay length of the exponential tail of the profile. To determine the scaled profile,  $C(r)/C_{\max} = f_c(r)$ , the parameters  $x_c$ ,  $x_w$  and  $\lambda_c$  are divided by  $L_a$ , so that  $r_c = x_c/L_a$ ,  $r_w = x_w/L_a$  and  $\phi_c = \lambda_c/L_a$ . Scaling of the signaling profile implies that  $r_c$ ,  $r_w$  and  $\phi_c$  are constant for different  $L_a$ .

Using the fit function for  $C(x)$  we calculate the corresponding growth profile  $g(x)$  using equation 6, which is given by

$$g_x(x) = \begin{cases} g_{\max} \left( 1 - \frac{(x - x_c - x_w)^2}{x_w^2} \right) e^{\frac{\gamma(x - x_c - x_w)^3}{3\lambda_c x_w^2} - \frac{\gamma(x - x_c - x_w)}{\lambda_c}} & \text{for } 0 \leq x \leq x_c + x_w \\ g_{\max} e^{-\frac{\gamma(x - x_c - x_w)}{\lambda_c}} & \text{for } x > x_c + x_w \end{cases}$$

$$\text{where } g_{\max} = \frac{v_s \gamma}{\lambda_c} e^{-\frac{2x_w \gamma}{3\lambda_c}} \quad (\text{supplementary equation 2}).$$

In addition to the fit parameters of  $f_c(x)$ , there are two new fit parameters:  $g_{\max}$ , which is approximately (but not exactly) equal to the amplitude, and  $\gamma$  (equation 2). The parameter  $g_{\max}$  is constrained by the other parameters and the source velocity. Therefore the source velocity  $v_s$  can be calculated from the known values of fit parameters (supplementary equation 2 and Table S2). This value of the source velocity is thus obtained independently of the measured value. Supplementary equation 2 can be scaled with respect to  $L_a$  in the same way as described for supplementary equation 1 above. For the simultaneous fit of  $f_c$  and  $g$  to profiles obtained in wildtype,  $\gamma$  was a free fit parameter, and  $\alpha = \frac{\ln 2}{\gamma(1+\varepsilon)}$  was calculated from this parameter with  $\varepsilon = 1$  (Fig. S1A, Fig. 1E, equation 2).

With these equations, the fit to wildtype data performs very well ( $R^2 = 0.96$ ; Fig. S1A), but slightly over-estimates the distance between the P-Mad and PH3 peaks. This may reflect the fact that the decision to undergo mitosis according to the temporal growth rule was made some time before cells became PH3-positive, during which time cells have moved towards the posterior. This means that the measured mitotic profile is slightly shifted to the posterior compared to the actual mitotic-decision-making profile. To account for a delay corresponding to a shift in the

proliferation profile, an additional parameter was introduced in the  $g(x)$  fit function to shift the profile along the  $x$ -axis:  $x = x + x_{shift}$ . Note that a shift along this axis in principle only affects the distance between the peaks – it has no direct effect on the value of  $\alpha$ , because  $\alpha$  is constrained by the decay of proliferation and concentration profiles,  $\lambda_g = \lambda_c / \gamma$  (supplementary equations 1 and 2). However, as the shift allows for a better fit of the decay (compare Fig. 2F and Fig. S1A), the value of  $\alpha$  obtained with this fit is probably more accurate than in a fit without shift. The delay  $\tau$  between the decision to undergo mitosis and the appearance of PH3 can be estimated as  $\tau \approx x_{shift} / v_s$ , which in wildtype corresponds to approximately 1 hour.

For fits in the mutant conditions,  $\alpha$  was set to 0.60 to test whether the data is consistent with the temporal model. This means that  $\gamma$  was fixed and that in these cases there were five fit parameters:  $r_c$ ,  $r_w$ ,  $r_{shift}$ ,  $\phi_c$  and  $g_{max}$ . After a first simultaneous fit of both signaling and growth profiles,  $g(r)$  was normalized to  $g_{max}$ . Then  $C/C_{max}$  and  $g/g_{max}$  profiles were fit simultaneously with only four parameters:  $r_c$ ,  $r_w$ ,  $r_{shift}$ , and  $\phi_c$ . The parameters  $r_c$ ,  $r_w$  and  $r_{shift}$  determine the position and distance between peaks, and the fit parameter  $\phi_c$  together with the set  $\gamma$  determines the decay length of the proliferation rate anterior to the mitotic peak. When fitting the profiles for C765>Dpp, the equations were modified to include an offset, corresponding to the signaling level at the edge of the disc. This offset was measured and not fit.

### Statistical analysis

For linear fits of the source velocity  $v_s$  and the anisotropy  $\epsilon$ , the standard error  $\sigma_s$  was estimated from 67% confidence intervals returned by the fit programme (the curve



fitting tool in matlab). The goodness of the fit,  $R^2$ , for a given set of fit parameters is defined as 1 minus the residual sum of squares divided by the total sum of squares and thus indicates how well the given model can explain the variation in the data. For the simultaneous fits, an error  $\sigma_a$  for a fit parameter  $a$  of the fit function  $f$  was obtained from the dependence of the  $R^2$  on the parameter  $a$  as follows:

$$\sigma_a = \pm \sqrt{\frac{-0.05 R_{opt}}{\frac{1}{2} \frac{d^2 R(a)}{da^2} \Big|_{a=a_{opt}}}} \quad (\text{supplementary equation 3}).$$

Here  $R(a)$  is the  $R^2$  as a function of  $a$  and  $R_{opt}$  is the  $R^2$  of the fit with the optimal fit parameter value  $a_{opt}$ . The factor 0.05 comes from the definition of a threshold of the  $R^2$  below which the fit is no longer considered good. This threshold is defined as 95% of  $R_{opt}$ .

## Theory

**The contribution of the second mitotic wave to the increase of the posterior compartment width can be neglected.**

This can be shown as follows: Posterior cells in the second mitotic wave reportedly divide only once, and not all cells divide. We estimate that the width of the posterior region,  $L_p$ , increases linearly due to this single cell division, in addition to an increase in width due to the movement of the source. The posterior width would thus be given by:

$$L_p = v_s t + v_p t \quad (\text{supplementary equation 4}).$$

The first term in supplementary equation 4 describes the increase in posterior width due to source movement (which is approximately linear, Fig. 1D), and the second term describes an increase in posterior width due to cell division in the posterior. This contribution is also approximately linear since posterior cells divide at most once. The expansion velocity due to growth in x-direction,  $v_p$ , is bounded by:

$$v_p < \frac{ap}{\theta} \quad (\text{supplementary equation 5}).$$

Here  $a$  is the cell diameter ( $a < 2\mu\text{m}$ ; as estimated from images),  $p$  is the percentage of cells that do divide in the second mitotic wave posterior to the furrow ( $p < 1$ , because not all cells divide, and those that do, divide only once) and  $\theta$  is the cell cycle length ( $\theta \geq 5h$ ; estimated from the shortest cell cycle length in the anterior). In addition, part of the growth will be absorbed in y-direction and will therefore not contribute to the increase of  $L_p$ ; as a consequence,  $ap/\theta$  constitutes an upper bound for  $v_p$ . The estimates for  $a$ ,  $p$  and  $\theta$  yield  $v_p < 0.4\mu\text{m}/h$ , which is small compared to  $v_s \approx 3\mu\text{m}/h$ . Therefore, the contribution of the second mitotic wave to the increase in the posterior width can be neglected.

**Derivation of equation 3.** From  $C(x,t) = C_{\max}(t)f(x,t)$  (equation 1), it follows that

$C_{\text{cell}}(t) = C_{\max}(t)f(x_{\text{cell}}(t),t)$ . The relative time derivative is given by

$\frac{\dot{C}_{\text{cell}}}{C_{\text{cell}}} = \frac{\dot{C}_{\max}}{C_{\max}} + \frac{\dot{f}}{f}$ , which for a profile that scales can be written as:

$$\frac{\dot{C}_{\text{cell}}}{C_{\text{cell}}} = \frac{\dot{C}_{\max}}{C_{\max}} + \frac{1}{f} \frac{dr_{\text{cell}}}{dt} \frac{df}{dr_{\text{cell}}} \quad (\text{supplementary equation 6}),$$

where,  $r_{cell} = x_{cell} / L_a$ . Therefore,  $\frac{dr_{cell}}{dt} = \frac{\dot{x}_{cell} L_a - x_{cell} \dot{L}_a}{L_a^2}$ , and  $\frac{df}{dr_{cell}} = L_a \frac{df}{dx_{cell}}$ . As a consequence,

$$\frac{\dot{C}_{cell}}{C_{cell}} = \frac{\dot{C}_{max}}{C_{max}} + \left( \dot{x}_{cell} - x_{cell} \frac{\dot{L}_a}{L_a} \right) \frac{\partial_x f}{f} \Big|_{x=x_{cell}} \quad (\text{supplementary equation 7}).$$

With  $v_{cell} = \dot{x}_{cell}$ , and  $\frac{\partial_x C}{C} = \frac{\partial_x f}{f}$ , this yields equation 3. Note that supplementary equation 7 and equation 3 apply to both wing and eye discs.

**Derivation of equation 5.** From equation 4, it follows that  $g_x = \partial_x v_g$ , while equation 2 postulates that  $g_x = \gamma \frac{\dot{C}_{cell}}{C_{cell}}$ . Together with the expression for  $\dot{C}_{cell} / C_{cell}$  given by supplementary equation 7, this results in

$$\partial_x v_g = \gamma \left( \frac{\dot{C}_{max}}{C_{max}} + \left( v_g - v_s - x_{cell} \frac{\dot{L}_a}{L_a} \right) \frac{\partial_x C}{C} \Big|_{x=x_{cell}} \right) \quad (\text{supplementary equation 8}).$$

Here we used  $v_{cell} = v_g - v_s$  (equation 4). Because  $C_{max}$  is proportional to  $L_a$  (Fig. S1C), it follows that, when  $\dot{L}_a \approx 0$ ,  $\dot{C}_{max} \approx 0$ , and supplementary equation 8 is reduced to equation 5. Note that supplementary equation 8 applies to both wing and eye discs, whereas the simplification of  $\dot{L}_a \approx 0$  and equation 5 only apply in the eye disc.

**Derivation of equation 6.** We rewrite and integrate equation 5 in the following way:

$$\int_0^{v_g(x)} \frac{dv_g}{(v_g - v_s)} = \gamma \int_{C_{\max}}^{C(x)} \frac{dC}{C} \quad (\text{supplementary equation 9}).$$

Here we make use of the fact that at for positions  $x < x_c$ ,  $v_g(x) = 0$ , because at this positions,  $\partial_x C$  is positive, resulting in negative  $\dot{C}_{cell} / C_{cell}$  (see supplementary equation 7) and therefore no growth. Therefore, supplementary equation 9 yields:

$$v_g(x) = v_s \left( 1 - \left( \frac{C(x)}{C_{\max}} \right)^\gamma \right) \quad (\text{supplementary equation 10}).$$

Because  $g_x = \partial_x v_g$  (equation 4), we can obtain an equation for  $g_x(x)$  by deriving supplementary equation 10 with respect to  $x$ . This yields equation 6. Note that supplementary equation 10 and equation 6 only apply in the eye disc.

### **Data analysis of the timecourse after start of furrow movement (Fig. S1L-P and Supplementary Movie 1)**

From the mean P-Mad (or Hairy) profiles quantified as a function of position ( $x$ ) at different times ( $t$ ), a **continuous concentration profile**  $C(x, t)$  was reconstructed by interpolation (as described previously (Wartlick et al. 2011c) (Fig. S1N). From the quantified mitotic density profiles, a **continuous proliferation profile**  $g_x(x, t)$  was obtained accordingly (Fig. S1O). Changes of cell positions in the growing tissue during time increments  $dt$  were then calculated based on equation 4:

$$x_{cell}(t + dt) = x_{cell}(t) + \left( \int_0^{x_{cell}} g_x(x, t) dx \right) dt - V_s dt \quad (\text{supplementary equation 11})$$

to obtain time courses of cell positions. The second and third term correspond to the effects of proliferation and furrow movement on cell position, respectively: growth increases the distance between a cell and the furrow, whereas furrow movement

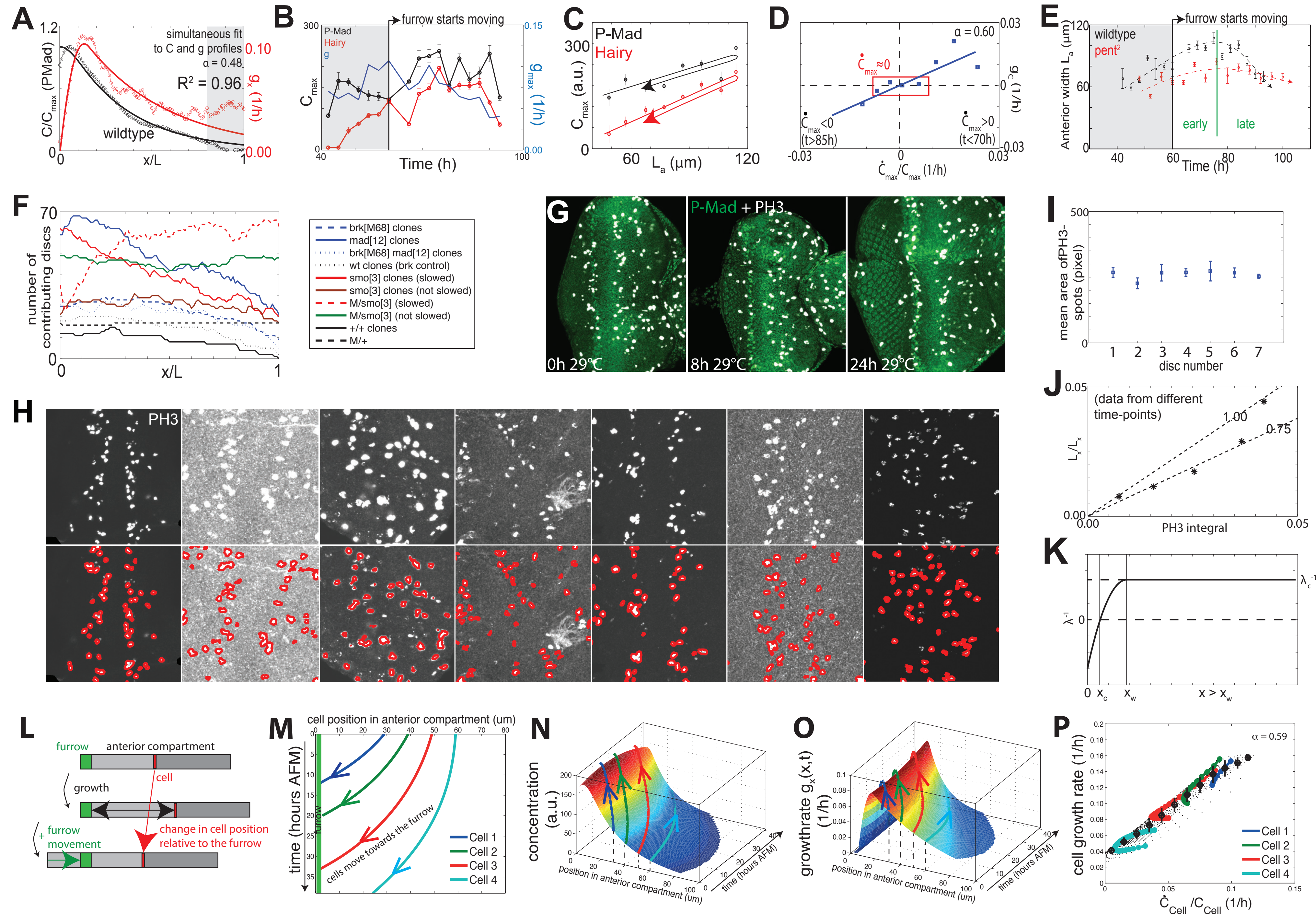


diminishes this distance (Fig. S1L). The resultant **cell positions over time**,  $x_{cell}(t)$ , are shown in Figure S1M. The **cellular concentration over time** was obtained from  $C(x,t)$  with  $C_{cell}(t) = C(x_{cell}(t),t)$  (Fig. S1N). The **cellular proliferation rate over time** was obtained from  $g_x(x,t)$  with  $g_{cell}(t) = (1 + \varepsilon) g_x(x_{cell}(t),t)$ , using the measured anisotropy  $\varepsilon \approx 1$  (Fig. 1E; Figure S1O). The relationship between cellular concentration and cellular proliferation rates can then be explored. For the  $g(\dot{C}/C)$  plot in Figure S1P,  $\dot{C}_{cell}/C_{cell}$  was calculated from  $C_{cell}(t)$  at different times and plotted against  $g_{cell}$  of these same times. The corresponding  $\alpha=0.59$  was obtained from the slope  $s$  of a linear fit with  $\alpha = \frac{\ln 2}{s}$  (equation 2).

## Supplementary Figure Legends

**Figure S1. Supplementary data and methods.** **A**, simultaneous fit to  $C/C_{max}$  and  $g$  without shift; the fit performs well but over-estimates the position between peaks, indicating that the proliferation profile may be shifted slightly; **B**,  $C_{max}$  of P-Mad and Hairy, as well as  $g_{max}$  over time; **C**, P-Mad and Hairy amplitude as a function of anterior width; arrows indicate trends (note that during development, the anterior width increases and then decreases (Fig. 1D)); **D**, the growth rate  $g_c$  is the component of the growth rate that is due to changes in  $\dot{C}_{max}$ , and was obtained from the fits of the proliferation data at different times of development (see Fig. 2E), using the fact that for  $x \rightarrow L_a$ , the value of  $\dot{C}_{cell}/C_{cell} \rightarrow \dot{C}_{max}/C_{max}$  (equation 3) and therefore  $g \rightarrow g_c$  (equation 2). Therefore, an approximate value of  $g_c$  can be obtained from the fitted  $g(L_a)$ . Values of  $\dot{C}_{max}/C_{max}$  at the same developmental times were obtained from the experimental  $C_{max}$  data (Fig. S1B). Note that the relationship between  $g_c$  and  $\dot{C}_{max}/C_{max}$  is linear, consistent with a temporal model (equation 2) and consistent with a value of  $\alpha$  of 60% (blue line). The red box indicates data-points from developmental times where  $\dot{C}_{max} \approx 0$ . **E**, anterior width over time in pent mutants (red) compared to wildtype; **F**, sample size for clonal analyses (Fig. 3 and 4) as a function of relative position; a “contributing disc” has a clone or tissue of the specified genotype that covers the position in question; **G**,  $hh^{ts2}/TM6B$  controls for the  $hh^{ts}$  experiment shown in Fig 4A; **H-I**, general method for detection of PH3-positive spots (**H**), generating binary images with spots of roughly equal area (red overlay on the original image in lower panel in **H**; see Supplementary Information); the mean area of spots per image is shown in **I**; **J**, calibration for conversion of mitotic density (PH3) into  $g_x$  (see Supplementary Information); **K**, the function  $\lambda^{-1}$  used to construct the fit function (see Supplementary Information). **L**, cell movement in the anterior region is affected by growth, which pushes cells away from the furrow, and furrow movement into the anterior, which reduces the distance between cells and the furrow. **M**, Cell trajectories can be calculated using the average growth profiles measured by PH3 staining and the measured furrow velocity (see supplementary material). Four sample cell trajectories are shown. **N**, **O**, continuous concentration and growth profiles as interpolated from the measured P-Mad and PH3 profiles. Cells that move in the tissue experience certain P-Mad concentrations (**N**) and exhibit certain cell growth rates (**O**), as illustrated by the four sample cell trajectories calculated in **M**. The growth rates shown here are actual growth rates,  $g = (1 + \epsilon) g_x$  (equation 2), taking the measured anisotropy (Fig. 1E) into account. **P**, cell growth rates (based on **O**) and temporal changes in cell concentrations (based on **N**) are linearly related, with  $\alpha=0.59$ . The four sample cells of S1M are shown in addition the behaviour of many more cells (small black dots) and their average (larger black circles).



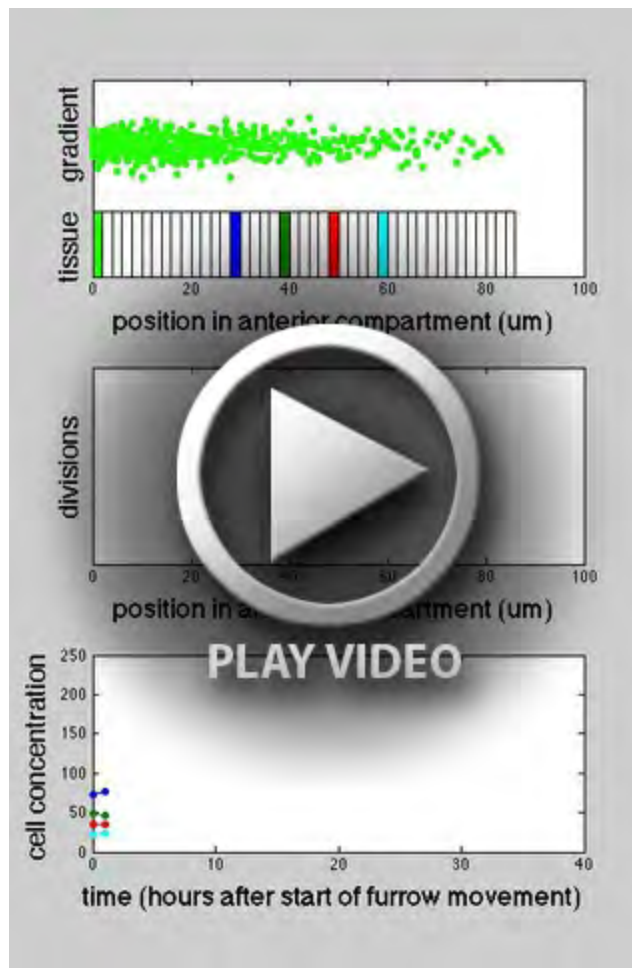


Supplementary Figure 1.



**Supplementary Movie 1.** This movie shows the data shown in Figure S1L-P in animated form, so is based on actual measured data. Top panel: each molecule is presented by a dot, and the gradient is represented by the number of dots as a function of position. The gradient scales with the size of the growing and shrinking tissue below it. In this tissue, four cells are marked: these cells move in the tissue over time according to the trajectories which were calculated in Fig. S1M. Bottom panel: As the cells move to different positions in the gradient, they experience different concentrations, which are tracked here over time (see also Fig. S1N). In the temporal model, cells divide when the concentration they perceive has increased by about 60%. These division events are marked by a star in all three panels. Note that 1) cell divisions are more likely to occur close to the furrow as cell concentrations increase markedly, and 2) cells which are positioned in the very anterior (for example the light blue cell and cells anterior to it), do not experience a large increase in concentration for much of development, and therefore do not divide often. Overall these effects lead to an accumulation of division events in front of the furrow (middle panel).





**Supplementary Movie 1.**

**Table S1. Parameters used in the paper.**

Parameters	Meaning	
$L_a$	anterior width	measured
$L_p$	posterior width	measured
$L_x = L_a + L_p$	total width in x-direction	measured
$L_y$	total width in y-direction	measured
$g_x$	growth rate in x-direction	extracted from fit to $L_x(t)$
$g_y$	growth rate in y-direction	extracted from fit to $L_y(t)$
$g = g_x + g_y$	growth rate	N/A
$\varepsilon = g_y / g_x$	anisotropy	extracted from fit to $\ln(L_y) = \varepsilon \ln(L_x)$
$x$	distance to the source	measured
$x_{cell}$	cell position with respect to the source	could be calculated with equation 4
$r = x / L_a$	relative distance to the source	calculated from $x$ and $L_a$
$t$	time (after hatching)	measured
$C$	P-Mad or Hairy concentration	measured
$\dot{C}$	time derivative of $C$	could be calculated from a fit to $C$
$\partial_x C$	spatial derivative of $C$	measured
$C_{max}$	amplitude of the concentration profile	measured
$\lambda_c$	decay length of the exponential tail of the concentration profile $C(x)$	extracted from fit to $C(r)$ or from simultaneous fit to $C(r)/C_{max}$ and $g(r)$
$\phi_c = \lambda_c / L_a$	decay length of the exponential tail of the relative concentration profile $C(r)$	extracted from fit to $C(r)$ or from simultaneous fit to $C(r)/C_{max}$ and $g(r)$
$r_c = x_c / L_a$	relative position of the maximum of the concentration profile $C(r)$	extracted from fit to $C(r)$ or from simultaneous fit to $C(r)/C_{max}$ and $g(r)$
$r_g = x_g / L_a$	relative position of the mitotic peak	numerical estimation based on fit to $g(r)$ or simultaneous fit to $C(r)/C_{max}$ and $g(r)$
$\gamma = \frac{\ln 2}{\alpha(1 + \varepsilon)}$	parameter of the temporal growth model, incorporating growth anisotropy	extracted from simultaneous fit to $C(r)/C_{max}$ and $g(r)$
$\alpha$	percentage by which signaling levels increase during one cell cycle	extracted from $\gamma$
$\lambda_g = \lambda_c / \gamma$	decay length of the exponential tail of the proliferation profile $g(x)$	extracted from simultaneous fit to $C(r)/C_{max}$ and $g(r)$
$\phi_g = \lambda_g / L_a$	decay length of the exponential tail of the proliferation profile $g(r)$	extracted from simultaneous fit to $C(r)/C_{max}$ and $g(r)$
$v_s \approx \dot{L}_p / L_p$	source velocity	extracted from fit to $L_p(t)$ or from simultaneous fit to $C(r)/C_{max}$ and $g(r)$
$v_g$	velocity field due to growth	could be calculated with equation 4 or with supplementary equation 10
$v_{cell} = v_g - v_s$	cell velocity	could be calculated from $v_s$ and $v_g$
$g_{max} = v_s \gamma / (\phi_c L_a)$	amplitude of proliferation profile	measured (based on PH3 profile) or extracted from simultaneous fit to $C(r)/C_{max}$ and $g(r)$
$r_{shift}$	shift between the mitotic decision making profile and the PH3 profile	extracted from simultaneous fit to $C(r)/C_{max}$ and $g(r)$
$\tau = r_{shift} L_a / v_s$	delay interval between decision to undergo mitosis and appearance of PH3	calculated from simultaneous fit parameters $r_{shift}$ and $v_s$ and the measured $L_a$

**Table S2. Parameter values.**

	wildtype	pent <sup>2</sup>	C765>Dpp	mad <sup>l2</sup>	brk <sup>M68</sup>	mad <sup>l2</sup> brk <sup>M68</sup>
R <sup>2</sup>	0.95	0.95	0.89	0.91	0.91	0.87
r <sub>c</sub>	0.09±0.03	0.09±0.02	0.15±0.02	0.08±0.01	0.16±0.02	0.08±0.01
r <sub>w</sub>	0.13±0.06	0.09±0.05	0.15±0.09	0.06±0.04	0.18±0.06	0.04±0.03
r <sub>shift</sub>	0.08±0.04	0.10±0.02	0.10±0.03	0.08±0.02	0.13±0.03	0.05±0.01
φ <sub>c</sub>	0.23±0.06	0.18±0.05	0.16±0.05 (fit with offset=0.47)	0.18±0.04	0.32±0.07	0.25±0.05
α (set value)	N/A	0.60	0.60	0.60	0.60	0.60
α <sub>Hairy</sub> (fit value)	0.71±0.25	0.87±0.31	0.59±0.64	0.69±0.22	0.50±0.16	0.62±0.17
α <sub>PMad</sub> (fit value)	0.57±0.19	0.75±0.26	0.52±0.43	N/A	N/A	N/A
g <sub>max</sub>	0.07	0.10	0.12	0.10	0.09	0.16
L <sub>a</sub>	(84±16) μm	(60±12) μm	(75±15) μm	(76±13) μm	(49±7) μm	(82±11) μm
ε	1.09±0.03	1.04±0.04	1.0	1.0	1.0	1.0
v <sub>s</sub> (measured)	(3.1±0.3) μm/h	(2.1±0.2) μm/h	N/A	N/A	N/A	N/A
v <sub>s</sub> (calculated)	2.9 μm/h	2.2 μm/h	3.6 μm/h	2.8 μm/h	3.1 μm/h	6.1 μm/h
delay (calculated)	(2.2±0.1) h	(2.7±0.2) h	(2.3±0.2) h	(2.2±0.2) h	(2.1±0.1) h	(0.6±0.6) h

**Table S2. Parameter values.** Parameters for simultaneous fits to  $C(r)$  and  $g(r)$  profiles shown in Fig. 2F,I,L, Fig. 4D,H,L, based on equation 6 (see Supplementary Information for fit function), as well as other, measured parameters. For wildtype, pent<sup>2</sup> and C765>Dpp fits both P-Mad and Hairy profiles were used; for mad<sup>l2</sup>, brk<sup>M68</sup> and mad<sup>l2</sup> brk<sup>M68</sup>, Hairy profiles were used. White shading: value given by the simultaneous fit; purple shading: set values; gray shading: measured values; dark gray shading: values calculated from fit parameters and/or measured values. For the fits shown in Fig. 2I,L, Fig. 4D,H,L, the value of α was set to 0.60 (set value). The value of α obtained from an unconstrained fit is also given in the table (fit value). Errors for simultaneous fit parameters were calculated as described in the Supplementary Information.